The following pages report the document:

A. Amicarelli, 2025, RANS SPH CFD for Air Quality: a closure on the turbulent Schmidt number constrained to Taylor's theory, paper preprint, protocol RS2501, pp.1-36.

RANS SPH CFD for Air Quality: a closure on the turbulent Schmidt number constrained to Taylor's theory

author: Andrea Amicarelli, freelance, Lucca (Italy), andrea.amicarelli@gmail.com

Abstract (max.150 words)
A closure of the mean-concentration Balance Equation on the turbulent Schmidt number Sc_T is formulated for a Lagrangian deterministic RANS CFD-SPH code on Air Quality (CFD-OUT-sweePDF v.2.0.0, Amicarelli et al.). It is constrained to Taylor's theory, involves velocity autocorrelation, is derived under Stationary Homogenous Isotropic Turbulence (StHIT) and applies under general conditions. Sc_T-StHIT closure is validated in a turbulent shear flow and a confined flow past a wall-mounted obstacle. Sc_T-StHIT reproduces the near-source 'ballistic regime' and corrects the mean concentration assessed with a state-of-the-art constant Sc_T up to one order of magnitude. Sc_T-StHIT fills most of the gap between deterministic and stochastic RANS CFD in simulating the mean concentration of a passive pollutant in a shear flow. An Eulerian variant is proposed. Sc_T-StHIT might interest any numerical method, RANS-SPDF, the turbulent Prandtl number and the LES Sub-Grid-Scale Sc_T. The SPH quadrature formulae and reconstruction schemes of the code are specified.

Keywords (5–10)
RANS CFD; turbulent Schmidt number; Air Quality; velocity autocorrelation; Sc_T-StHIT turbulence closure; Sub-Particle Pollutant Source; mean concentration; SPH quadrature formulae; spatial reconstruction schemes; CFD-OUT-sweePDF.

1. INTRODUCTION

In deterministic Reynolds-Averaged Navier-Stokes (RANS) modelling, the turbulent Schmidt number Sc_T is defined as the ratio between the turbulent viscosity ν_T (m^2/s) and the coefficient of turbulent dispersion K_T (m^2/s) of the transported scalar or pollutant. Sc_T plays a major role in the diffusion terms of the Balance Equations (BEs) for the concentration mean $\overline{C}$ and variance. Sc_T is systematically assumed constant ('Sc_T-const approach') by deterministic RANS CFD codes (i.e. RANS CFD codes based on mean-velocity trajectories). It is equivalent to setting Sc_T to an intermediate value approximately used all over the domain. Tominaga & Stathopoulos (2007, [1]) reported that RANS CFD studies had been globally used a range of Sc_T values going from 0.2 to 1.3. Some specific Sc_T reference values are listed hereafter: Sc_T=0.72 (Efthimiou et al., 2017, [2]; Venetsanos et al., 2010, [3]; Violeau, 2009, [4]); Sc_T=0.63 (Hsieh et al., 2007, [5]); Sc_T=0.70 (Dong et al., 2017, [6]; Issakhov et al., 2020, [7]); Sc_T=0.80 (experimental value from Fackrell & Robins, 1982, [8]); Sc_T=0.90 (Baik et al., 2007, [9]; Tominaga et al., 2013, [10]; experimental value from Yee & Biltoft, 2004 [11]). Despite being a state-of-the-art common practise, the adoption of any constant Sc_T value determines a systematic overestimation/underestimation of K_T at small/large flight times since the Pollutant Source PS. This reduced accuracy in reproducing the turbulent flux of the pollutant mass, due to the absence of velocity autocorrelation in Sc_T-const approach, represents the leading difference between stochastic and deterministic RANS models in simulating the mean concentration. In the following, these model categories are compared by highlighting their differences, no matter about the numerical method used to discretise the BEs.

Deterministic RANS models (e.g. Efthimiou et al., 2017, [2]) assess the concentration ensemble mean and rarely the ensemble variance. A sole set of computational nodes considers both the transporting fluid and the transported scalar. No effect of velocity autocorrelation is taken into account (Sc_T-const approach). Mean velocity, mean Turbulent Kinetic Energy (TKE) and mean pressure are the main target variables of the simulated air-flow. Either 1st-order or 2nd-order turbulence closures are considered, being the latter rarely adopted for Air Quality. Limited accuracy is obtained under 2nd-order kinetics via the segregation coefficient. Deterministic RANS models are commonly and effectively applied to Air Quality and Water Quality.

RANS-PDF (Probability Density Function; Pope, 1985, [12]) models represent the most accurate category of stochastic RANS models for turbulent flows with scalar dispersion. Two sets of computational nodes are used via a Particle-in-Cell approach. A complementary solver is needed to assess the mean-pressure gradient in the Stochastic Differential Equation (SDE, e.g. Morkisz & Przybylowicz, 2017, [13]) for velocity. RANS-PDF simulates instantaneous-like quantities and is constrained to an accurate reproduction of both velocity autocorrelation and RANS Reynolds' stress Balance Equation (RS-BE); e.g. the Simplified Langevin Model is coherent with the return-to-isotropy Rotta's RS-BE model. Any ensemble statistic and the pdfs of velocity and concentration are directly estimated. Second-order kinetics are accurately represented. Stochastic RANS models usually apply to combustion processes, but rarely to Air Quality, except for Bahlali et al. (2018, [14]) and Bahlali et al. (2019, [15]), where RANS-PDF is used as LSM (Lagrangian Stochastic Models; e.g. Thomson, 1987, [26]). RANS-LSM is the category of stochastic RANS models most commonly used for Air Quality (e.g. Gariazzo et al., 2004, [16]): they exclusively target concentration and require the velocity statistics in input.
The aim of the present study is to make deterministic RANS models fill a relevant part of the accuracy gap they experience with respect to stochastic RANS models in representing the mean concentration. A closure of the RANS BE for $\overline{C}$ (Cm-BE) on the turbulent Schmidt number is presented as 'Sc_T-StHIT'; it is derived under Stationary Homogeneous Isotropic Turbulence, but applies under general conditions using local values of the turbulent quantities. Sc_T-StHIT is constrained to Taylor's theory (Taylor, 1922, [17]) to model the effects of velocity autocorrelation and is written as the default Sc_T approach of the code CFD-OUT-sweePDF v.2.0.0 (Amicarelli et al.). It is a Lagrangian deterministic RANS CFD-SPH code for turbulent flows with pollutant dispersion. The aforementioned constant value Sc_T=0.72, used in the previous version of the code (Amicarelli, 2024, [18]) for any test case, is here activated only for sparring simulations. The mathematical and numerical models of Sc_T-StHIT are proposed for both Lagrangian and Eulerian deterministic RANS CFD codes. A secondary and separate validation involves the Sub-Particle Pollutant Source (SPPS) scheme. It is a new 'sub-grid' spatial reconstruction scheme for $\overline{C}$ working in a very limited region just downstream the PS.
The present paper is organised as follows. The code CFD-OUT-sweePDF v.2.0.0 is synthetically described (Sec.2). For sake of brevity, only some detailed descriptions of the features of the previous code version were reported in Amicarelli (2024, [18]). They concerned: time integration; the criteria on the PDE stability, physical bounds and convergence; the Wall Functions WFs. Other code features validated in Amicarelli (2024, [18]) are described in the current paper, as they are active and further tested with the new simulations. It is the Smoothed Particle Hydrodynamics (SPH) quadrature formulae (Sec.3) and the spatial reconstruction schemes for the mean pressure, the mean TKE and the mean concentration at the PS (Sec.4). It follows the presentation of the main novelties of the current code version: the turbulence closure Sc_T-StHIT of the Balance Equation for the mean concentration (Sec.5) and the SPPS scheme (Sec.6). For sake of brevity, the missing descriptions are reported in a following study (Amicarelli, 2025, [19]); they concern the mathematical models of the BEs, the SPH Time-Space Ensemble (SPH-TSE) filter, the stabilisation term in the Momentum Equation and the inlet/outlet sections. The code novelties are validated on two test cases by comparison with the available measurements (Fackrell & Robins, 1982, [8]), the numerical results of a stochastic RANS-LSM model (Amicarelli et al., 2011, [20]) and the previous code version (Amicarelli, 2024, [18]). These incremental validations involve an experimental turbulent shear flow with elevated PS (Sec.7) and a confined turbulent flow past a wall-mounted cubic obstacle with Canyon PS (Sec.8). The original contributions of the current study are cited in the abstract and the conclusions (Sec.9). Some general pre-processing procedures are reported in appendix (Sec.10). Simulations are executed under reduced pressure for barotropic neutrally-buoyant micro-scale air-flows following Amicarelli (2024, [18]) as for the management of Initial Conditions (IC) and stationary conditions. The background pressure is adopted analogously to Isik & He (2021, [21]).

2. THE CODE CFD-OUT-SWEEPDF V.2.0.0

CFD-OUT-sweePDF v.2.0.0 (Amicarelli et al.) is a deterministic Lagrangian RANS CFD-SPH code for turbulent flows with pollutant transport. The following applications have been investigated: Outdoor Air Quality (OAQ), Indoor Air Quality (IAQ) and air-treatment processes for Duct Air Quality (DAQ). They include ordinary stack emissions and accidental releases. The simulated obstacles and buildings are isolated structures or parts of a complex matrix like an Urban Canopy of several tenths of street canyons. The code reproduces any useful spatial resolution under a maximum spatial cover of 2km×2km×0.5km. Non-stationary and stationary conditions are directly simulated, whereas many state-of-the-art RANS CFD studies efficiently apply extrapolation algorithms as an alternative to a direct representation of transient regimes (e.g., Galindo et al., 2019, [22]).

The code adopts the Weakly-Compressible (WC) approach to assess the mean pressure, with turbulent transport term in the RANS Continuity Equation (RANS-CE). The code relies on Kato & Launder's improved k-eps model (Kat&Lau-k-eps), being considered one of the most accurate 2-equation 1st-order turbulence closures, and on the mean-concentration Balance Equation (BE). Its closure 'Sc_T-StHIT' concerns the turbulent Schmidt number, is constrained to Taylor's theory (Taylor, 1922, [17]) and reproduces the effects of velocity autocorrelation. The semi-implicit Euler's scheme and forward-backward Euler's schemes rule time integration, merging a spatial linear filter, a stabilisation term in the Momentum Equation and the shell SPH filter to enhance the stability domains. The SPH Time-Space Ensemble (SPH-TSE) filter improves the accuracy of the ensemble statistics under specific conditions. Any RANS-SPH formula is valid at any *Re*; alternative Implicit Large Eddy Simulation (ILES-SPH) and Navier-Stokes (NS-SPH) formulations are also available. The code is written in Fortran 95 and has not been distributed. Further details follow hereafter.

The application of the SPH filters $\langle\ \rangle$ and the semi-implicit Euler's scheme to the RANS Momentum Equation (RANS-ME) and the Trajectory Equation (TE), traced by the mean motion of the computational particle '$_0$', provides the following Partial-Differential-Equation (PDE) scheme:

$$\underline{\overline{u}}_{0,k+1}=\underline{\overline{u}}_{0,k}+\left\{\begin{array}{l}\underline{g}-\frac{1}{\overline{\rho}_0}\left\langle\underline{\nabla}\overline{p}\right\rangle_{C1,0}-\frac{2}{3}\left\langle\underline{\nabla}\overline{q}\right\rangle_{C1,0}+\left\langle\underline{\nabla}\cdot\left[\left(\nu_T+\overline{\nu}\right)\left(\underline{\nabla}\otimes\underline{\overline{u}}\right)^T\right]\right\rangle_{C0,0}+\\-2\left(1-c_{TB}\right)\max\left\{\left(\frac{\overline{p}_0}{\overline{\rho}_0}+\frac{2}{3}\overline{q}_0\right);0\right\}\left\langle\underline{\nabla}1\right\rangle_{C-1,0}\end{array}\right\}_k\Delta t_k \qquad (2.1)$$

$$\underline{x}_{0,k+1}=\underline{x}_{0,k}+\underline{\overline{u}}_{0,k+1}\Delta t_k$$

where $\underline{\overline{u}}$ (m/s) is the mean velocity vector, $\underline{g}$ (m/s^2) is the gravitational acceleration, $\overline{p}$ (Pa) is the mean pressure, $\overline{\rho}$ (kg/m^3) is the mean density, $\overline{q}$ (m^2/s^2) is the mean Turbulent Kinetic Energy (TKE), ν_T (m^2/s) is the turbulent viscosity, $\overline{\nu}$ (m^2/s) is the mean kinematic viscosity, t (s) is time, Δt (s) is the time step duration, the subscript '$_k$' indicates the time step and $\underline{x}$ (m) is the particle position. The subscripts '$_{C-1}$', '$_{C0}$' and '$_{C1}$' denote C_{-1}-, C_0- and C_1-consistent SPH filters. The last term within curl brackets in (2.1) is the 'ME stabilisation term' and also inhibits the so-called SPH tensile instability (Vignjevic & Campbell, 2009, [23]) thanks to its null limiter. This term plays an analogous role to SPH Particle Shifting Techniques (e.g. Crespo et al., 2008, [24]; Aristodemo et al., 2015, [25]; Cui et al., 2020, [26]) since both reduce the deformations of the control volumes (Fang et al., 2017, [27]). Only close to some simplified outlet sections '$_{TB}$', the truncated portion of the SPH kernel support is not reconstructed: here the stability constant c_{TB} is non-null, the limiter above is deactivated and C_0 consistency is set.

Analogously to the WC approach for ILES-SPH (e.g., Cui et al., 2019, [28]; Tagliafierro et al., 2022, [29]), the SPH RANS-CE is used to assess the mean pressure via a barotropic Equation of State, which is averaged after Reynolds. The WC approach is alternative to keeping density constant and applying any algorithm for pressure-velocity coupling (e.g., Issakhov & Baitureyeva, 2019, [30]). The SPH filters and the forward-backward Euler's scheme with linear filter applies to RANS-CE as:

$$\overline{\rho}_{0,k+1,PRE} = \overline{\rho}_{0,k} + \left[-\overline{\rho}_{0,k} \left\langle \underline{\nabla} \cdot \overline{\underline{u}} \right\rangle_{C1,0,k+1} + \left\langle \underline{\nabla} \cdot \left(\nu_{T,k+1} \underline{\nabla} \overline{\rho}_k \right) \right\rangle_{C0,0} \right] \Delta t_k ,$$
$$\overline{\rho}_{0,k+1} = \left(1-\theta_{0,k+1}\right) \overline{\rho}_{0,k+1,PRE} + \theta_{0,k+1} \left\langle \overline{\rho}_{k+1,PRE} \right\rangle_{C0,0} ,$$
$$\theta_{k+1} = \frac{\left(c_1 \frac{c_{ref}}{h} - 2 \frac{c_2 \nu_{T,k+1}}{h^2} \right) \Delta t_k}{\left(1 - W_{k+1} \omega_{k+1}\right) \left(1 + c_1 \frac{c_{ref}}{h} \Delta t_k \right) - 2 \frac{c_2 \nu_{T,k+1}}{h^2} \Delta t_k} \tag{2.2}$$

where θ is the RANS-SPH smoothing coefficient, c_{ref} (m/s) is the sound speed at the reference state, W (m^{-3}) is the SPH kernel function, ω (m^3) is the particle volume, h (m) is the kernel support size, the subscript '$_{PRE}$' indicates the predictor stage, c_1 and c_2 are derived from stability analyses.
The application of the SPH filters and a forward-backward Euler's scheme, stabilised by the shell SPH filter, to the RANS Balance Equation for the mean Turbulent Kinetic Energy (TKE-BE) provides the following PDE scheme:

$$\overline{q}_{0,k+1} = \frac{\overline{q}_{0,k} + \left(\left\langle P_q \right\rangle_{SH*,C1,0,k} + \left\langle D_q \right\rangle_{SH*,C0,0,k} \right) \Delta t_k}{\left(1 + \frac{\overline{\varepsilon}_{0,k}}{\overline{q}_{0,k}} \Delta t \right)} ,$$
$$\left\langle D_q \right\rangle_{SH*,C0,0} = \left\langle \underline{\nabla} \cdot \left[\left(\nu_T + \overline{\nu} \right) \left(\underline{\nabla} \overline{q} \right) \right] \right\rangle_{SH*,C0,0} , \quad \left\langle P_q \right\rangle_{SH*,C1,0} = 4 \nu_{T,0,SHq} \sqrt{\left(- \left\langle S_m \right\rangle_{C1,0} \right) \left\langle R_m \right\rangle_{C1,0}} \tag{2.3}$$

$\left\langle P_q \right\rangle$ (m^2/s^3), $\left\langle D_q \right\rangle$ (m^2/s^3) and $\overline{\varepsilon}$ (m^2/s^3) are the production, diffusion and dissipation rates of the mean TKE. S_m (s^{-2}) and R_m (s^{-2}) are the quadratic invariants of the mean strain-rate tensor and of the mean rotation tensor. The subscript '$_{SH*}$' indicates that, in the formulation of the turbulent viscosity, $\overline{q}$ is replaced by its shell SPH filter, i.e. the SPH filter net of the contribution of the computational node. Instead, where the subscript '$_{SHq}$' is used, $\overline{q}$ is always replaced by its shell SPH approximation.
The application of the SPH filters and the forward-backward Euler's scheme (version of Leroy et al., 2014, [31]) to the BE of the mean-TKE dissipation rate (eps-BE) provides the following PDE scheme:

$$\overline{\varepsilon}_{0,k+1} = \frac{\overline{\varepsilon}_{0,k} + \left(\left\langle P_\varepsilon \right\rangle_{C1,0,k} + \left\langle D_\varepsilon \right\rangle_{C0,0,k} \right) \Delta t_k}{\left(1 + C_{\varepsilon_2} \frac{\overline{\varepsilon}_{0,k}}{\overline{q}_{0,k}} \Delta t \right)} ,$$
$$\left\langle D_\varepsilon \right\rangle_{C0,0} = \left\langle \underline{\nabla} \cdot \left[\left(\frac{\nu_T}{\sigma_\varepsilon} + \overline{\nu} \right) \left(\underline{\nabla} \overline{\varepsilon} \right) \right] \right\rangle_{C0,0} , \quad \left\langle P_\varepsilon \right\rangle_{C1,0} = 4 C_\mu C_{\varepsilon_1} \overline{q}_0 \sqrt{\left(- \left\langle S_m \right\rangle_{C1,0} \right) \left\langle R_m \right\rangle_{C1,0}} \tag{2.4}$$

where $\left\langle P_\varepsilon \right\rangle$ (m^2/s^4) and $\left\langle D_\varepsilon \right\rangle$ (m^2/s^4) are the SPH eps-BE production and dissipation terms. The constants $\left(C_\mu, \sigma_\varepsilon, C_{\varepsilon_1}, C_{\varepsilon_2} \right)$ are defined by Launder & Spalding (1974, [32]). The constants of any RANS turbulence closure are derived under equilibrium turbulence, represent relevant approximations under non-equilibrium conditions typical of complex flows and thus they might be reformulated in future studies, following the investigations in Fang et al. (2017, [33]).
No explicit filtering technique for WC high-frequency acoustic waves (e.g. Chen et al., 2022, [34]) is adopted. These numerical waves are damped by the combined effect of the SPH-TSE filter, the SPH RANS-CE time scheme, the stabilisation effect of θ and the acoustic convergence criterion $\Delta t_{AW} \equiv 0.10 F_{\Delta t} \frac{2h}{c_{ref} + \left| \underline{u} \right|_{\max}}$, where $F_{\Delta t}$ is the optimisation factor (Amicarelli, 2024, [18]).

The application of the SPH filters and a variant of the forward-backward Euler's scheme to the BE for the mean concentration $\overline{C}$ (kg/m^3) of a passive pollutant provides the following scheme:

$$\overline{C}_{0,k+1} = \overline{C}_{0,k} + \left\langle \underline{\nabla} \cdot \left[\left(D_M + \frac{\nu_{T,k+1}}{Sc_{T,k+1}} \right) \underline{\nabla} \overline{C}_k \right] \right\rangle_{C0,0} \Delta t_k \tag{2.5}$$

where D_M (m^2/s) is the coefficient of molecular diffusion and Sc_T is the turbulent Schmidt number. The associated turbulence closure 'Sc_T-StHIT' is constrained to Taylor's theory (Taylor, 1922, [17]) and provides Sc_T with the following closed-form solution:

$$Sc_{T,k+1} = \frac{\frac{9}{8} C_\mu \tilde{C}_{0,k+1}}{\left[1 - \frac{T_{L,k+1}}{\breve{t}_{FP,k+1}} \left(1 - e^{-\frac{\breve{t}_{FP,k+1}}{T_{L,k+1}}} \right) \right]}, \quad \lim_{\breve{t}_{FP} \to 0} Sc_T = \infty, \quad \lim_{\breve{t}_{FP} \gg T_L} Sc_T = \frac{9}{8} C_\mu \tilde{C}_0 \tag{2.6}$$

where $\breve{t}_{FP}$ (s) is the weighted ensemble mean of the pollutant flight time, T_L (s) is the Lagrangian integral time scale of turbulence and $\tilde{C}_0$ is the peak value of the compensated velocity Lagrangian structure function. Sc_T-StHIT models the effects of velocity autocorrelation thus inhibiting the systematic error of the state-of-the-art deterministic CFD codes in assessing $\overline{C}$ under constant Sc_T.
The code relies on a tenth of original stability conditions and physical-bound conditions for the PDE schemes presented above, including stabilisation terms and Δt-dependent conditions. They are formulated for several blends of forward-backward Euler's time schemes with/without filters, under linear or quadratic-hyperbolic rate of change. Eight convergence criteria for time integration are built on the non-redundant Δt-dependent conditions.
The SPH Time-Space Ensemble (SPH-TSE) filter combines the SPH (spatial) kernel with an exponential-decaying SPH time kernel of memory-loss factor a_{mem}. The ensemble mean of a generic quantity A is the weighted sum of the spatial filter over the RANS TKE-averaged eddy size among all the turbulent vortices l_0 (m) and the ensemble mean at the previous time step, at the same point:

$$\left. \overline{A} \right|_k \simeq a_{mem,k} \left\langle A \right\rangle_{l_0,k} + \left(1 - a_{mem,k} \right) \left. \overline{A} \right|_{k-1}; \quad a_{mem,k} \simeq \begin{cases} 1 - e^{-3\frac{\min\{\Delta t_k, T_{L,k}\}}{T_{L,k}}}, & T_{L,k} \le \left(t_k - t_{IC} \right) \\ 1 - e^{-3\frac{\min\{\Delta t_k, (t_k - t_{IC})\}}{(t_k - t_{IC})}}, & 0 < \left(t_k - t_{IC} \right) < T_{L,k} \end{cases} \tag{2.7}$$

where the subscript '$_{IC}$' denotes Initial Conditions. Under RANS-SPH simulations, the SPH-TSE filter corrects the ensemble statistics during the post-processing stage of the code algorithm and its difference with the SPH filter feeds a convergence criterion to stationary conditions. Under ILES-SPH simulations, the SPH-TSE filter is also used to convert the output LES-filtered quantities into Reynolds' ensemble statistics and to assess the higher-order ensemble moments, the ensemble probability density function and the ensemble cumulative density function. The ensemble statistics for Solid Dynamics are computed via the SPH time filter. In other turbulence approaches, the SPH-TSE filter might convert the output instantaneous-like quantities into Reynolds' statistics.
The SPH filter applies to all the derivatives in the BEs and to the functions needing filtering. The SPH filters of a generic function, gradient and 'quasi-Laplacian' (i.e. the divergence of the product of the function gradient by a scalar g) consider contributions from fluid particles '$_b$', solid particles '$_s$' and fixed-wall elements '$_w$' in the SPH neighbourhood of the computational particle. The SPH filter of the gradient of a generic function f is represented by a C_1-consistent SPH quadrature formula:

$$\left\langle \underline{\nabla} f \right\rangle_{C1,0} = \underline{\underline{B}}_0 \left\{ \sum_b \left(f_b - f_0 \right) \underline{\nabla} W_b \omega_b + \sum_s \left(f_{0s} - f_0 \right) \underline{\nabla} W_s \omega_s + \right. \tag{2.8}$$

$$+\sum_{w}\left(f_{0w}-f_0\right)\underline{\underline{T}}_w\underline{G}_{c,0w}+\sum_{w}\left\{\underline{\underline{T}}_w\left\{\underline{\underline{G}}_{l,0w}\left[\underline{\underline{T}}_w^T\left(\underline{\nabla}f\right)_{0w}\right]\right\}\right\}\Bigg\}$$

where $\underline{\underline{B}}_0$ is a renormalisation matrix, built with inner and boundary terms, and $\underline{\underline{T}}_w$ is the matrix of the directional cosines of the fixed-wall element.
The SPH filter of the quasi-Laplacian is a C_0-consistent SPH quadrature formula:

$$\left\langle\underline{\nabla}\cdot\left[g\underline{\nabla}f\right]\right\rangle_{C0,0}=-2g_0\sum_{b\neq 0}\frac{2\overline{\rho}_{b*}g_b}{\overline{\rho}_0 g_0+\overline{\rho}_b g_b}\frac{\left(f_b-f_0\right)}{r_{0b}}\left.\frac{\partial W}{\partial r}\right|_b\omega_b+$$
$$-2g_0\sum_{s\neq 0}\frac{\left(f_{0s}-f_0\right)}{r_{0s}}\left.\frac{\partial W}{\partial r}\right|_s\omega_s-2g_0\sum_{w}\left(f_{0w}-f_0\right)L_{c,0w};\quad \overline{\rho}_{b*}\equiv\begin{cases}0.5\left(\overline{\rho}_0+\overline{\rho}_b\right), & f\equiv\overline{C}\\ \overline{\rho}_b, & otherwise\end{cases} \tag{2.9}$$

where r (m) is the distance from the computational particle. The mathematical expression of the fluid-fluid interaction term in (2.9) is a generalisation of a mathematical formula in Di Monaco et al. (2011, [35]). Specific C_1-consistent quadrature formulae apply to positioning-grid barycentres and monitoring points. A kernel-based anti-cluster strategy is used for fluid-fluid and fluid-body interactions. A unified anti-cluster and anti-penetration strategy applies to fluid-wall interactions, based on reactions as numerical collisions. Eq.(2.9) exactly conserves the pollutant mass.
A series of spatial reconstruction schemes applies, included RANS SPH Wall Functions (WFs) and the Sub-Particle Pollutant-Source (SPPS) scheme. WFs depend on three hydraulic-roughness regimes, and the depths of the turbulent Boundary Layer (BL) and of the Neutral Surface BL (NSBL); TKE-BE is adapted to $\overline{\varepsilon}$ WF.
Under fluid flows confined by solid rigid boundaries, the conservative Balance Equation for the particle Control Volume (CV-BE) can be activated to exactly conserve the fluid global volume. CV-BE time integration is ruled by a simple forward-backward Euler's scheme with a post-correction.
$\underline{G}_{c,0w}$ (m^{-1}), $\underline{\underline{G}}_{l,0w}$ and $L_{c,0w}$ (m^{-2}) in (2.8) and (2.9) are geometrical quadrature formulae over a single fixed-wall element: they are mentioned in Sec.3.4. Newton-Euler's equations rule Computational Solid Dynamics (CSD). The main parts of those source lines of the current code dealing with Newton-Euler's equations are imported from the code SPHERA v.10.0.0 (RSE SpA, 2022, [36]) and were presented in Amicarelli et al. (2015, [37]), Amicarelli et al. (2020, [38]), Amicarelli et al. (2021, [39]) and Amicarelli et al. (2022, [40]). The solid-body quantities are interpreted as instantaneous and interact with the fluid mean variables. Ensemble averaging only applies to solid bodies under post-processing. The integration of CSD SPH and CFD SPH is alternative to coupling the latter with a CSD solver: such numerical solution is used in many ILES- CFD-SPH studies (e.g., Tagliafierro et al., 2021, [41]).
The main improvement introduced in CFD-OUT-sweePDF v.2.0.0 with respect to the previous code version is the Sc_T-StHIT closure; secondary novelties concern the SPPS scheme, the truncation outlet sections '$_{TB}$', the conservative variant to the SPH filter of the quasi-Laplacian in SPH Cm-BE and a correction to the roughness length z_0 (m) in the intermediate hydraulic-roughness regime. This is now expressed as $z_0=\frac{\left(70-\mathrm{Re}_*\right)}{\left(70-5\right)}\frac{\overline{\nu}}{9u_*}+\frac{\left(\mathrm{Re}_*-5\right)}{\left(70-5\right)}\frac{H_{sgr}}{5}$, where u_* (m/s) is the friction velocity (at ground), Re_* is the friction Reynolds number and H_{sgr} (m) is the sub-grid roughness.

3. SPH QUADRATURE FORMULAE

The SPH filter applies to the derivatives of the governing BEs of (2.1)-(2.5). The SPH spatial filters of a generic function (Sec.3.1), gradient (Sec.3.2) and 'quasi-Laplacian' (Sec.3.3) consider contributions from fluid particles, solid particles and fixed-wall elements. The latter also depend on geometrical quadrature formulae over a single fixed-wall element (Sec.3.4). A unified anti-cluster and anti-penetration strategy for fluid-wall interactions is represented by reactions modelled as numerical collisions (Sec.3.5, Sec.3.6). The anti-cluster strategy for fluid-fluid and fluid-body interactions (Sec.3.7) is based on a cubic anti-cluster kernel. The SPH quadrature formulae rely on the assessment of relative positions, kernel functions and gradients (Sec.3.7), and are also computed over the barycentres of the positioning grid and the monitoring points (Sec.3.8). Any SPH filter is interpreted as a spatial filter in the continuum plus a 3D open weighted quadrature formula for given irregular nodes (Sec.3.9). The formulations for all the SPH-TSE ensemble statistics and the SPH spatial statistics are completed in Sec.3.10. Each vector component is processed as a generic scalar.

3.1. SPH spatial filter of a generic function

The SPH filter of a generic function f around the computational particle '$_0$' is represented by the following C_1-consistent SPH quadrature formula:

$$\left\langle f\right\rangle_0 = \left\langle f\right\rangle_{C1,0} = \frac{\left\langle f\right\rangle_{C-1,0}}{\sigma_0} + \left\langle \frac{\partial f}{\partial x_j}\right\rangle_{C1,0}\left(x_{j,0} - \frac{\left\langle x_j\right\rangle_{C-1,0}}{\sigma_0}\right), \quad \sigma_0 \equiv \left\langle 1\right\rangle_{C-1,0} \tag{3.1}$$

where σ is the discrete Shepard's coefficient and the C_{-1} SPH quadrature formula is the straightforward discretisation of the integral SPH filter:

$$\left\langle f\right\rangle_{C-1,0} = \sum_b f_b W_b \omega_b + \sum_s f_{0s} W_s \omega_s + \sum_w f_{0w} F_{c,0w} + \sum_w \underline{\underline{T}}_w \left\{\underline{\underline{F}}_{l,0w}\left[\underline{\underline{T}}_w^T \left(\underline{\nabla} f\right)_{0w}\right]\right\} \tag{3.2}$$

where the summations of the first line are executed over the volumes ω of the neighbouring fluid '$_b$' and solid '$_s$' particles which locally discretise the fluid domain and the solid bodies. The fluid-body interaction quantities '$_{0s}$' are synthesized in Sec.3.10 and Sec.4. The following two terms are associated with a summation over the neighbouring elements '$_w$' of the fixed walls. The first one represents the quadrature formula for the constant term of the linear Taylor series of f over the portion of the kernel support truncated by the set of the neighbouring fixed-wall elements $V_{h,w}^{'}$ (m^3). The last term is associated with the linear term of the same series. The fixed-wall 'constant' term depends on the constant boundary function f_{0w} (Sec.3.10) and a geometrical quadrature formula over a single-wall element $F_{c,0w}$ (Sec.3.4). The fixed-wall 'linear' term considers the constant boundary gradient $\left(\underline{\nabla} f\right)_{0w}$ (Sec.3.10) and the matrix $\underline{\underline{F}}_{l,0w}$ (m) of the following geometrical quadrature formula over a single wall element, which depends on the portions of solid angle α_S:

$$\underline{\underline{F}}_{l,0w} = \left(\sum_{\Delta\alpha_S}\left(\underline{\nabla} r \otimes \underline{\nabla} r\right) I_3 \Delta\alpha_S\right)_{0w}, \quad I_3 \equiv \int_{r_{0w}}^{2h} r^3 W dr \tag{3.3}$$

Eq.(3.3) is here formulated, but not used for sake of simplicity. The omission of the fixed-wall 'linear' term is equivalent to assume a null gradient over $V_{h,w}^{'}$. The alternative fixed-wall terms in 2D read:

$$\sum_w f_{0w,2D} F_{c,0w,2D} + \sum_w \left(\underline{\nabla} f\right)_{0w} \cdot \left(\underline{i}_w F_{l1,0w,2D} + \underline{n}_w F_{l2,0w,2D}\right) \tag{3.4}$$

where $\underline{n}_w$ is the wall-element normal and $\underline{i}_w$ is its perpendicular unit vector. The geometrical quadrature formulae $F_{c,0w,2D}$, $F_{l1,0w,2D}$ (m) and $F_{l2,0w,2D}$ (m) for the fixed-wall constant and linear 2D terms are mentioned in Sec.3.4. The 2D fixed-wall constant $f_{0w,2D}$ assumes the following form:

$$f_{0w,2D} = f_0 + \left(\underline{\nabla} f\right)_{0w} \cdot \left(\underline{x}_{0w} - \underline{x}_0\right) \tag{3.5}$$

where $\underline{x}_{0w}$ (m) is the closest position along the wall element '$_w$' to the computational particle '$_0$'.

3.2. SPH spatial filter of the gradient of a generic function

The SPH filter of a gradient is represented by the C_1-consistent SPH quadrature formula (2.8).
The inverse of the renormalisation matrix $\underline{\underline{B}}_0$ is the opposite of the C_0-consistent SPH filter of the gradient of the position of the numerical neighbours (Randles & Libertsky, 1996, [42]):

$$\underline{\underline{B}}_0^{-1} \equiv -\left\langle \underline{\nabla} \otimes \underline{x} \right\rangle_{C0,0} \Leftrightarrow B_{ij,0}^{-1} \equiv -\left\langle \frac{\partial x_j}{\partial x_i} \right\rangle_{C0,0} \tag{3.6}$$

and here includes boundary contributions. In the continuum, it equals the opposite of the identity matrix, which replaces (3.6) if $\underline{\underline{B}}_0^{-1}$ is bad-conditioned ($\left|\underline{\underline{B}}_0^{-1}\right| < 1\times10^{-4}$). The C_0-consistent SPH filter:

$$\left\langle \underline{\nabla} f \right\rangle_{C1,0} = -\underline{\underline{B}}_0 \left\langle \underline{\nabla} f \right\rangle_{C0,0}, \quad \left\langle \underline{\nabla} f \right\rangle_{C0,0} \equiv \left\langle \underline{\nabla}\left(f - f_0\right) \right\rangle_{C-1,0} \tag{3.7}$$

depends on the C_{-1} SPH quadrature formula of the integral SPH filter after integration over the fluid, solid-body and fixed-wall subdomains:

$$\left\langle \underline{\nabla} f \right\rangle_{C-1,0} = -\sum_b f_b \underline{\nabla} W_b \omega_b - \sum_s f_{0s} \underline{\nabla} W_s \omega_s - \sum_w f_{0w} \underline{\underline{T}}_w \underline{G}_{c,0w} - \sum_w \left\{ \underline{\underline{T}}_w \left\{ \underline{\underline{G}}_{l,0w} \left[\underline{\underline{T}}_w^T \left(\underline{\nabla} f \right)_{0w} \right] \right\} \right\} \tag{3.8}$$

The corresponding 2D fixed-wall terms for (2.8) read:

$$-\underline{\underline{B}}_0 \left[\sum_w \left(f_{0w,2D} - f_0 \right) \underline{n}_w G_{c,0w,2D} + \sum_w \left(\underline{\nabla} f \right)_{0w} G_{l,0w,2D} \right] \tag{3.9}$$

The geometrical quadrature formulae over a single fixed-wall element $\underline{G}_{c,0w}$ (m^{-1}) and $\underline{\underline{G}}_{l,0w}$ for the fixed-wall constant and linear terms are mentioned in Sec.3.4, together with the corresponding 2D geometrical quadrature formulae $G_{c,0w,2D}$ and $G_{l,0w,2D}$.

3.3. SPH spatial filter of the 'quasi-Laplacian' of a generic function

The SPH filter of the divergence of the product of a function gradient by a generic scalar g is mentioned as 'quasi-Laplacian' of the function, for sake of simplicity. If the scalar is uniform, the divergence is equal to the product of the scalar by the Laplacian. The SPH filter of the quasi-Laplacian of a function is represented by the C_0-consistent SPH quadrature formula (2.9). It is an extension of the mathematical formula for the inner viscous term of the Momentum Equation reported in Di Monaco et al. (2011, [35]), after the integration of the BC terms and a conservative variant for Cm-BE. The inner term of (2.9) is a combination of Cleary's and Morris' formulations (Basa et al., 2009, [43]): the three expressions are equal under homogeneous conditions for the mean density and the scalar. Basa et al. (2009, [43]) demonstrated it is a hybrid SPH-FDM operator, where FDM stands for Finite Difference Method. The linear fixed-wall term is null for sake of simplicity without deteriorating the consistency order. However, under the BCs of Sec.3.10, such term would be null. The integral over a single fixed-wall element $L_{c,0w}$ (m^{-2}) is mentioned in Sec.3.4. The filter (2.9) exactly conserves the pollutant mass in every pair-particle subsystem.

3.4. Geometrical quadrature formulae over a single fixed-wall element

This section does not represent an original contribution of the current code: it is mentioned for sake of completeness. The fixed-wall contributions to the SPH quadrature formulae of Sec.3.1-Sec.3.3 also depend on the following geometrical quadrature formulae over a single fixed-wall element: $F_{c,0w}$, $F_{c,0w,2D}$, $F_{l1,0w,2D}$, $F_{l2,0w,2D}$, $\underline{G}_{c,0w}$, $\underline{\underline{G}}_{l,0w}$, $G_{c,0w,2D}$, $G_{l,0w,2D}$ and $L_{c,0w}$. Five of them apply in 2D, the other four in 3D. The main parts of those source lines of the current code dealing with the above-mentioned formulae are imported from the code SPHERA v.10.0.0 (RSE SpA, 2022, [36]) and were presented in Di Monaco et al. (2011, [35]).

3.5. Fluid-wall reactions over fixed-wall faces

The anti-cluster strategy for fluid-fluid and fluid-body interactions, based on the application of the cubic anti-cluster kernel, does not apply to the interactions between fluid and fixed walls (or 'fluid-wall interactions', for sake of simplicity) for two reasons. The first is to simplify the algorithm not introducing formulae in Sec.3.4, which relies on the cubic beta-spline kernel. The latter is to represent symmetry conditions without fluid-wall penetrations, under the approximated and fast BC treatment for fixed walls. This need is not shown by the more accurate but slower BC treatment for solid bodies. The solution is the simulation of fluid-wall reactions represented by numerical collisions. They are as smooth as possible in time and space not to alter the fluid fields in the inner domain. The global fluid-wall reaction $\underline{R}_{FW}$ (kg×m×s^{-2}) for a computational particle interests the neighbouring fixed-wall faces, coherently with the mathematical formula in Di Monaco et al. (2011, [35]):

$$\underline{R}_{FW,0} = \sum_w \underline{R}_{FW,0w} = -m_0 \frac{c_{ref}^2}{h} \sum_w \frac{\underline{r}_{0w}}{|\underline{r}|_{0w}} \cdot \begin{cases} -\ln\left[\dfrac{h+\left(d_{0w}-d_{FW,\max}\right)}{h}\right], d_{0w} < d_{FW,\max}, \ \bar{u}_{0n} > 0 \\ 0, \ otherwise \end{cases} ; \tag{3.10}$$

$$d_{FW,\max} \equiv \frac{\Delta x}{4}; \ \bar{u}_{0n} \equiv \underline{\bar{u}}_0 \cdot \underline{n}_w$$

provided that the particle lies within the collision zone of depth $d_{FW,max}$ (m), is approaching the fixed-wall element and meets the wall-face ‘projection visibility criterion’. This is satisfied if the projection of the particle position over the plane/line containing the fixed-wall element in 3D/2D is internal to the element. The quantity Δx (m) is the particle size, whereas d (m) is any inter-element distance. The advantage of (3.10) is that its limited magnitude makes the approximated stability criterion on fluid-wall reactions (Amicarelli, 2024, [18]) provide an acceptable time discretisation without more constraining criteria, even if this strategy does not strictly guarantee the non-penetration condition under optimised simulations.

3.6. Fluid-wall reactions over fixed-wall edges

This section does not represent an original contribution of the current code: it is mentioned for sake of completeness. To improve the cover of the collision zone around a boundary made of fixed-wall elements, fluid-wall reactions are also computed over fixed-wall edges, only if no fluid-wall reaction is activated on the adjacent fixed-wall faces (Sec.3.5). The number of fluid-wall reactions for fixed-wall edges is normally at least 3 orders of magnitude smaller than the number of fluid-wall reactions for fixed-wall faces. The main parts of those source lines of the current code dealing with fluid-wall reactions for fixed-wall edges are imported from the code SPHERA v.10.0.0 (RSE SpA, 2022, [36]).

3.7. Relative positions, kernel functions and gradients

The current code uses the cubic beta-spline kernel, whose mathematical formulation was presented in Monaghan & Lattanzio (1985, [44]):

$$W = \begin{cases} \dfrac{1}{\pi h^3}\left(1-\dfrac{3}{2}q^2+\dfrac{3}{4}q^3\right), \ 0 \le q < 1 \\ \dfrac{1}{4\pi h^3}\left(2-q\right)^3, \ 1 \le q < 2 \\ 0, \ 2 \le q \end{cases} ; \ \underline{\nabla}W = \begin{cases} \dfrac{1}{\pi h^4}\left(\dfrac{9}{4}q^2-3q\right)\dfrac{\underline{r}}{r}, \ 0 \le q < 1 \\ -\dfrac{3}{4\pi h^4}\left(2-q\right)^2\dfrac{\underline{r}}{r}, \ 1 \le q < 2 \\ 0, \ 2 \le q \end{cases} ; \ q \equiv \frac{r}{h} \tag{3.11}$$

In 2D, W and $\underline{\nabla}W$ are multiplied by 10h/7. In the inner domain and over the solid bodies, the anti-cluster strategy replaces the kernel gradient of (3.11) in the terms of SPH RANS-ME with the gradient of the cubic anti-cluster kernel, which was mathematically defined in Gallati & Braschi (2000, [45]):

$$W = \begin{cases} \dfrac{15}{64\pi h^3}\left(2-q\right)^3, \ 0 \le q < 2 \\ 0, \ 2 \le q \end{cases} ; \ \underline{\nabla}W = \begin{cases} -\dfrac{45}{64\pi h^4}\left(2-q\right)^2\dfrac{\underline{r}}{r}, \ 0 \le q < 2 \\ 0, \ 2 \le q \end{cases} \tag{3.12}$$

Its kernel function applies to the SPH filter of several functions. In 2D, W and $\underline{\nabla}W$ are multiplied by $4h/3$. The most frequent kernel- and position-related interaction quantities are saved by default in dedicated arrays for fluid-fluid, fluid-body and body-body pair-particle interactions, unless specific pre-processor macros are activated to save the Total Virtual Memory *TVM* (GB) at the expense of the elapsed time t_{ela} (s). Some algorithm details are presented hereafter. The following 6 scalars are assessed and stored every time step, each fluid-fluid pair-particle interaction:

$$grad\_W\_fp0\_fpn(1:3) \equiv \underline{\nabla W}_{\beta s,0b};\ \ W\_fp0\_fpn = W_{\beta s,0b} \geq 0;$$

$$gW2\_by\_gW\_fp0\_fpn \equiv \begin{cases} \dfrac{\underline{\nabla W}_{ac,0b}}{\underline{\nabla W}_{\beta s,0b}} \geq 0, & \underline{\nabla W}_{\beta s,0b} \neq \underline{0} \\ 1, & \underline{\nabla W}_{\beta s,0b} = \underline{0} \end{cases};$$

$$x\_by\_gW\_fp0\_fpn \equiv \begin{cases} \dfrac{\underline{x}_b - \underline{x}_0}{\underline{\nabla W}_{\beta s,0b}} = -\dfrac{\left|\underline{x}_b - \underline{x}_0\right|}{\left|\underline{\nabla W}_{\beta s,0b}\right|} = \left(\dfrac{1}{r_{0b}} \left.\dfrac{\partial W_{\beta s}}{\partial r}\right|_{0b}\right)^{-1} < 0, & \underline{\nabla W}_{\beta s,0b} \neq \underline{0} \\ 1, & \underline{\nabla W}_{\beta s,0b} = \underline{0} \end{cases} \tag{3.13}$$

Considering the default value $h/\Delta x$=1.30, the average number of SPH fluid neighbours in 3D is ca.75, far from boundaries. The subscripts '$_{\beta s}$' and '$_{ac}$' refer to the beta-spline and the anti-cluster cubic kernels. The following 5 scalars are updated every time step, each fluid-body pair-particle interaction:

$$grad\_W\_fp0\_bpn(1:3) \equiv \underline{\nabla W}_{\beta s,0s};$$

$$gW2\_by\_gW\_fp0\_bpn \equiv \begin{cases} \dfrac{\underline{\nabla W}_{ac,0s}}{\underline{\nabla W}_{\beta s,0s}} \geq 0, & \underline{\nabla W}_{\beta s,0b} \neq \underline{0} \\ 1, & \underline{\nabla W}_{\beta s,0b} = \underline{0} \end{cases};$$

$$x\_by\_gW\_fp0\_bpn \equiv \begin{cases} \dfrac{\underline{x}_s - \underline{x}_0}{\underline{\nabla W}_{\beta s,0s}} = -\dfrac{\left|\underline{x}_s - \underline{x}_0\right|}{\left|\underline{\nabla W}_{\beta s,0s}\right|} = \left(\dfrac{1}{r_{0s}} \left.\dfrac{\partial W_{\beta s}}{\partial r}\right|_{0s}\right)^{-1} < 0, & \underline{\nabla W}_{\beta s,0s} \neq \underline{0} \\ 1, & \underline{\nabla W}_{\beta s,0s} = \underline{0} \end{cases} \tag{3.14}$$

The following 3 scalars are updated every time step, each body-body pair-particle interaction:

$$x\_bp0\_bpn(1:3) \equiv \underline{x}_{sb} - \underline{x}_{s0} \tag{3.15}$$

The subscripts '$_{s0}$' and '$_{sb}$' refer to the computational body particle and the neighbouring body particle, respectively. Any other kernel function is always computed on the fly. The activation of the pre-processor macro '*ON_THE_FLY_grad_W_fp0_fpn*' in compile-time makes '*grad_W_fp0_fpn*' be computed on the fly. The analogous activation of the macro '*ON_THE_FLY_OTHERS*' makes '*gW2_by_gW_fp0_fpn*', '*x_by_gW_fp0_fpn*' and '*W_fp0_fpn*' be computed on the fly as well.

3.8. SPH quadrature formulae for positioning-grid barycentres and monitoring points

For sake of efficiency in terms of *TVM* and t_{ela}, the C_1-consistent SPH quadrature formula used to assess a spatial average over a grid barycentre '$_{gp}$' or a monitoring point relies on the statistics already computed at the position of the nearest SPH particle '$_{np}$', boundary terms included:

$$\langle f \rangle_{C1,gp} = \frac{\langle f \rangle_{C-1,np}}{\sigma_{np}} + \left\langle \frac{\partial f}{\partial x_j} \right\rangle_{C1,np} \left(x_{j,gp} - \frac{\langle x_j \rangle_{C-1,np}}{\sigma_{np}} \right) \tag{3.16}$$

where Einstein's summation convention applies to the subscript '$_j$'. Eq.(3.16) is used in the memory-loss term of the SPH-TSE filter. Besides the SPH and SPH-TSE filters, even the nearest-particle method applies to monitoring points, for post-processing purposes, with the following motivation. Under almost-discontinuous spatial fields, the nearest-particle unfiltered 'raw' value at a generic monitoring point converges faster than the SPH and SPH-TSE filters: the 'raw' values are then preferred to avoid finer Δx. However, the nearest-particle method might be too inaccurate depending on the nearest-particle distance from the monitor and the field inhomogeneity. Thus, when using a 'raw' profile, the target field has to be almost discontinuous and a comparison with the associated SPH-TSE profile has to support the reliability of the profile obtained by the nearest-particle method.

3.9. SPH filter: a spatial filter in the continuum plus a 3D open weighted quadrature formula for given irregular nodes

Each of the three SPH filters (Sec.3.1–Sec.3.3) is interpreted as a spatial filter in the continuum '$\frown$' plus a 3D open weighted quadrature formula for given irregular nodes. The quadrature formula is open because the particle position strictly lies within the particle volume, not over its edges. The nodes are given because the particle trajectories are computed and not arbitrarily chosen, except for minor displacements induced by the stabilisation terms. The SPH filters are formally revised hereafter to demonstrate the interpretation above. A generic weighted quadrature formula reads:

$$\int_V f dV \simeq \sum_b f_b \gamma_b \tag{3.17}$$

where γ_b are the coefficients or weights computed over the nodes 'b', represented by the neighbouring particles in CFD-SPH. In the following, the definition (3.17) applies to the SPH filters for the function, the gradient and the quasi-Laplacian, far from boundaries for sake of synthesis.

The SPH filter for a generic function (3.1)–(3.2) is interpreted as a spatial filter in the continuum plus a C_1-consistent 3D open weighted quadrature formula for given irregular nodes:

$$\begin{gathered}\widehat{f}_{\underline{x}_0} = \int_{V_h} fWdV \simeq \sum_b f_b W_b \gamma_b, \quad \gamma_{b\neq 0} = \frac{\omega_b}{\sigma_0} + \frac{\left(\underline{\underline{B}}_0 \underline{\nabla} W_b \omega_b\right)}{W_b} \cdot \left(\underline{x}_0 - \frac{\sum_b \underline{x}_b W_b \omega_b}{\sigma_0} \right), \\ \gamma_{b=0} = \frac{\omega_0}{\sigma_0} - \frac{\left(\underline{\underline{B}}_0 \sum_{b\neq 0} \underline{\nabla} W_b \omega_b\right)}{W_0} \cdot \left(\underline{x}_0 - \frac{\sum_b \underline{x}_b W_b \omega_b}{\sigma_0} \right)\end{gathered} \tag{3.18}$$

where the convolution kernel is W. The analogous formula with Gaussian weights and chosen nodes is the C_1-consistent formula of Gauss-Hermite. Under ICs, the SPH nodes are set by the code in a regular Cartesian distribution to reduce the SPH truncation errors. Under these conditions and virtually assuming a top-hat kernel, not suggested for SPH simulations, the SPH quadrature formula (3.18) would be equivalent to a trilinear interpolation.

The SPH filter for the gradient of a generic function (2.8) is interpreted as a spatial filter of f in the continuum plus a C_1-consistent 3D open weighted quadrature formula for given irregular nodes:

$$\begin{gathered}\widehat{\underline{\nabla} f}_{\underline{x}_0} = \int_{V_h} \left(\underline{\nabla} f\right) WdV = -\int_{V_h} f\left(\underline{\nabla} W\right) dV \simeq \sum_b f_b \left(\nabla_i W\right)_b \gamma_{i,b}, \\ \gamma_{i,b\neq 0} = \frac{\left(\underline{\underline{B}}_0 \underline{\nabla} W_b\right)_i}{\left(\underline{\nabla} W_b\right)_i} \omega_b, \quad \left(\gamma \underline{\nabla} W\right)_{i,b=0} = -\left(\underline{\underline{B}}_0 \sum_{b\neq 0} \underline{\nabla} W_b \omega_b\right)_i, \quad i = 1,2,3\end{gathered} \tag{3.19}$$

where the convolution kernels are the opposites of the components 'i' of the SPH kernel gradient.

In 2D the boundary treatment of fixed walls of the code of Sec.2 relies on a different integration approach with respect to 3D, merging boundary surface and line integrals after a double integration by parts. The overall 2D integral SPH spatial filter of a gradient reads:

$$\left(\widehat{\underline{\nabla} f}\right)_{2D} = \int_{V_h} \left(\underline{\nabla} f\right) WdV = -\int_{V_{h,IN,BD}} \left(\underline{\nabla} W\right) fdV - f_0 \int_{A_h} W \underline{n} dA + \left(\underline{\nabla} f\right)_0 \int_{V_h'} WdV \tag{3.20}$$

where the subscripts '$_{IN}$' and '$_{BD}$' represent the fluid subdomain and the subdomain of the solid bodies, respectively, whereas A_h (m, 2D) is the intersection between the set of fixed-wall neighbours and the kernel support of the fluid computational particle.

Statistics	$\underline{f}_{0s}$	$\underline{f}_{0w}$	$\left(\underline{\nabla}\otimes\underline{f}\right)_{0w}$
$\left\langle \underline{\nabla}\cdot\left[\left(\overline{\nu}+\nu_T\right)\left(\underline{\nabla}\otimes\overline{\underline{u}}\right)^T\right]\right\rangle_{C0}$	$\overline{\underline{u}}_{0s}$	$\overline{\underline{u}}_{0w}$	$\underline{\underline{0}}$
$\left\langle\overline{\underline{u}}\right\rangle_{C1}, \left\langle\left(\underline{\nabla}\otimes\overline{\underline{u}}\right)^T\right\rangle_{C1}, \left\langle\underline{\nabla}\cdot\overline{\underline{u}}\right\rangle_{C1}, \left\langle\overline{\underline{u}}\right\rangle_{(h,T_L)}$	$\overline{\underline{u}}_{0s}$	$\overline{\underline{u}}_{0w}$	$\underline{\underline{0}}$
$\left\langle\overline{p}\right\rangle_{C1}, \left\langle\underline{\nabla}\overline{p}\right\rangle_{C1}, \left\langle\overline{p}\right\rangle_{(h,T_L)}$	$\overline{p}_{0s}$	$\overline{p}_{0w}$	$\left(\underline{\nabla}\overline{p}\right)_{0w}$
$\left\langle\underline{\nabla}\cdot\left(\frac{\nu_T}{\sigma_\rho}\underline{\nabla}\overline{\rho}\right)\right\rangle_{C0}$	$\overline{\rho}\left(\overline{p}_{0s}\right)$	$\overline{\rho}_0$	$\underline{0}$
$\left\langle\underline{\nabla}\cdot\left[\left(\overline{\nu}+\frac{\nu_T}{\sigma_q}\right)\underline{\nabla}\overline{q}\right]\right\rangle_{C0,SH*}$	$\overline{q}_0$	$\overline{q}_0$	$\underline{0}$
$\left\langle\underline{\nabla}\cdot\left[\left(\overline{\nu}+\frac{\nu_T}{\sigma_\varepsilon}\right)\underline{\nabla}\overline{\varepsilon}\right]\right\rangle_{C0}$	$\overline{\varepsilon}_0$	$\overline{\varepsilon}_0$	$\underline{0}$
$\left\langle\overline{q}\right\rangle_{C1}, \left\langle\overline{q}\right\rangle_{C0}, \left\langle\underline{\nabla}\overline{q}\right\rangle_{C1}, \left\langle\overline{q}\right\rangle_{(h,T_L)}$	$\overline{q}_{0s}$	$\overline{q}_0$	$\left(\underline{\nabla}\overline{q}\right)_{0w}$
$\left\langle\overline{\varepsilon}\right\rangle_{C1}, \left\langle\overline{\varepsilon}\right\rangle_{(h,T_L)}$	0	0	$\underline{0}$
$\left\langle\underline{\nabla}\cdot\left[\left(D_M+\frac{\nu_T}{Sc_T}\right)\underline{\nabla}\overline{C}\right]\right\rangle_{C0}$	$\overline{C}_0$	$\overline{C}_0$	$\underline{0}$
$\left\langle\overline{C}\right\rangle_{C1}, \left\langle\overline{C}\right\rangle_{(h,T_L)}$	0	0	$\underline{0}$
$\left\langle\underline{\nabla}1\right\rangle_{C-1}$	1	1	$\underline{0}$
$\left\langle\overline{p}\right\rangle_{C0}$	$\overline{p}_{0s}$	$\overline{p}_{0w}$	$\underline{0}$, 3D $\left(\underline{\nabla}\overline{p}\right)_{0w}$, 2D
$\left\langle\underline{\nabla}\otimes\underline{x}\right\rangle_{C0}$	$\underline{x}_s$	$\underline{x}_0$, 3D $\underline{x}_{0w}$, 2D	$\underline{\underline{I}}$
$\left\langle\breve{t}_{FP}\right\rangle_{C1}, \left\langle\breve{t}_{FP}\right\rangle_{(h,T_L)}$	0	0	$\underline{0}$
$\left\langle\underline{\nabla}\overline{p}\right\rangle_{REC}, \left\langle\underline{\nabla}\overline{q}\right\rangle_{REC}$	0	0	$\underline{0}$

Table 3.1. RANS SPH-TSE ensemble statistics and SPH spatial statistics. Column 1 (from left to right): list of the SPH spatial statistics at the positions of the fluid particles, monitors and grid barycentres, and the SPH-TSE ensemble statistics $\langle\ \rangle_{(h,T_L)}$ at the monitors and grid barycentres. Each group of statistics is associated with the boundary quantities formulated for solid bodies (column 2) and fixed walls (columns 3 and 4). The last row refers to the reconstructing '$_{REC}$' gradients used by the reconstruction schemes of Sec.4.

The SPH filter for the 'quasi-Laplacian' of a generic function (2.9) might be interpreted as a spatial filter in the continuum plus a C_0-consistent 3D open weighted quadrature formula for given irregular nodes, provided that one could find a more proper definition to the convolution kernel X:

$$\left(\overline{\underline{\nabla}\cdot\left[g\underline{\nabla}f\right]}\right)_{\underline{x}_0} = \int_{V_h}\left[\underline{\nabla}\cdot\left(g\underline{\nabla}f\right)\right]WdV \simeq \sum_b f_b X_b \gamma_b,\ \ (\gamma X)_{b\neq 0} = -4\frac{\overline{\rho}_b g_0 g_b}{g_0\overline{\rho}_0 + g_b\overline{\rho}_b}\frac{1}{r_{0b}}\left.\frac{\partial W}{\partial r}\right|_b \omega_b,$$
$$(\gamma X)_{b=0} = 2g_0\sum_{b\neq 0}\frac{2\overline{\rho}_b g_b}{g_0\overline{\rho}_0 + g_b\overline{\rho}_b}\frac{1}{r_{0b}}\left.\frac{\partial W}{\partial r}\right|_b \omega_b \Rightarrow \int_{V_h}\left[\underline{\nabla}\cdot\left(g\underline{\nabla}f\right)\right]WdV \simeq \int_{V_h} fXdV \tag{3.21}$$

3.10. RANS SPH-TSE ensemble statistics, SPH spatial statistics and boundary quantities

Table 3.1 shows the synthetic list of RANS SPH-TSE ensemble statistics and SPH spatial statistics with their boundary quantities. The spatial statistics are the applications of the SPH filters for functions (3.1)–(3.2), gradients (2.8) and quasi-Laplacians (2.9). The boundary quantities with double subscript in the last three columns are formulated either in the previous subsections or in Sec.4.

No assumption is needed on the SPH kernel to keep C_1-consistency in (2.8) and (3.1): any W can be used, included a hybrid combination of kernels. This implies the following conditions: the SPH filters of the mean-pressure and mean-TKE gradients are C_1-consistent, even if the cubic beta-spline kernel always applies beyond the fixed walls; the SPH filters of the mean pressure and the mean TKE are C_1-consistent even if computed with a kernel function slightly incoherent with its gradient, which is also hybrid (being partly 'beta-spline' beyond fixed walls, partly 'anti-cluster'). This approach is even justified by the role of the anti-cluster kernel, which is interpreted as an anti-cluster filter applied to the cubic beta-spline kernel in the inner domain and over the solid bodies.

4. SPATIAL RECONSTRUCTION SCHEMES FOR MEAN PRESSURE, TKE AND CONCENTRATION

The boundary values of the mean pressure, the mean TKE and their gradients (Table 3.1) are assessed by C_1-consistent spatial reconstruction schemes (Sec.4.1, Sec.4.2). They feature any point '$_{BC}$' in the outer portions of the SPH kernel support of the computational particle '$_0$' that lie in the solid subdomain. The boundary mean-TKE gradient is also needed by the reconstruction scheme for $\overline{p}_{BC}$. The spatial reconstruction scheme for the mean concentration at the PS is reported in Sec.4.3. The reconstruction schemes in RANS-SPH are analogous to the ILES-SPH reconstruction schemes but the first are free from any sub-particle energy dissipation, which is intrinsically related to the ILES-SPH Riemann's solvers (e.g., Gu et al., 2017, [46]).

4.1. C_1-consistent mean pressure and its gradient at fluid-solid interfaces

The spatial reconstruction scheme for the mean pressure and its gradient at fluid-solid interfaces is described in the following. Free-slip conditions at any fluid-solid interface are featured by in-built motion of the fluid '$_F$' and the solid '$_S$' sides along the wall normal $\underline{n}_{wall}$:

$$\underline{a}_{wall,F}\cdot\underline{n}_{wall} = \underline{a}_{wall,S}\cdot\underline{n}_{wall} \tag{4.1}$$

where $\underline{a}$ (m/s^2) is the acceleration. The subscript '$_{wall}$' refers to any fluid-solid interface including both solid bodies and fixed walls in the continuum, contrarily to '$_w$' which relates to a single discrete element of a fixed wall. All the kinematic quantities related to the solid subdomains are assumed as instantaneous and free from turbulent fluctuations during the resolution of the BEs of the fluid subdomain. The ensemble average of (4.1) is then obtained as follows:

$$\overline{\underline{a}_{wall,F}\cdot\underline{n}_{wall}} = \overline{\underline{a}_{wall,S}\cdot\underline{n}_{wall}} \Rightarrow \overline{\underline{a}}_{wall,F}\cdot\underline{n}_{wall} \simeq \underline{a}_{wall,S}\cdot\underline{n}_{wall} \tag{4.2}$$

After neglecting the diffusion term (contrarily to the ILES-SPH reconstruction scheme of Cercos-Pita et al., 2017, [47]) and assuming WC or incompressible conditions, the fluid mean acceleration reads:

$$\overline{\underline{a}}_{wall,F} = -\frac{1}{\left.\overline{\rho}\right|_{\underline{x}_{wall}}}\left.\underline{\nabla}\overline{p}\right|_{\underline{x}_{wall}} + \underline{g} - \frac{2}{3}\left(\nabla\overline{q}\right)_{\underline{x}_{wall}} \tag{4.3}$$

The linearity assumption for the mean-pressure field implies the following relationships:

$$\overline{p}_{BC} = \overline{p}_{wall} + \underline{\nabla}\overline{p}\Big|_{\underline{x}_{wall}} \cdot \left(\underline{x}_{BC} - \underline{x}_{wall}\right), \quad \overline{p}_0 = \overline{p}_{wall} + \underline{\nabla}\overline{p}\Big|_{\underline{x}_{wall}} \cdot \left(\underline{x}_0 - \underline{x}_{wall}\right) \tag{4.4}$$

The system (4.1)–(4.4) permits to derive an expression for the boundary mean pressure as follows:

$$\begin{aligned} \overline{p}_{BC} = \overline{p}_0 + \underline{\nabla}\overline{p}\Big|_{\underline{x}_{wall}} \cdot \left(\underline{x}_{BC} - \underline{x}_0\right) = \overline{p}_0 + \overline{\rho}_{wall}\left[\left(\underline{g} - \underline{a}_{wall,S} - \frac{2}{3}\left(\nabla\overline{q}\right)_{wall}\right) \cdot \underline{n}_{wall}\right]\underline{n}_{wall} \cdot \left(\underline{x}_{BC} - \underline{x}_0\right) \\ + \left\{\underline{\nabla}\overline{p}\Big|_{\underline{x}_{wall}} - \overline{\rho}_{wall}\left[\left(\underline{g} - \underline{a}_{wall,S} - \frac{2}{3}\left(\nabla\overline{q}\right)_{wall}\right) \cdot \underline{n}_{wall}\right]\underline{n}_{wall}\right\} \cdot \left(\underline{x}_{BC} - \underline{x}_0\right) \end{aligned} \tag{4.5}$$

Under C_1 consistency for $\overline{p}$, the following assumptions are also flawless:

$$\overline{\rho}_{wall} = \overline{\rho}_0, \quad \underline{a}_{wall,S} = \underline{a}_{BC}, \quad \underline{\nabla}\overline{p}\Big|_{\underline{x}_{wall}} = \underline{\nabla}\overline{p}\Big|_{\underline{x}_0}, \quad \left\langle\underline{\nabla}\overline{p}\right\rangle_0 = \left\langle\underline{\nabla}\overline{p}\right\rangle_{REC,0} \tag{4.6}$$

where $\left\langle\underline{\nabla}\overline{p}\right\rangle_{REC}$ (Pa/m) is the reconstructing '$_{REC}$' mean-pressure gradient. Under free-slip conditions, the tangential component of $\underline{\nabla}\overline{p}$ does not depend on the interface acceleration and symmetry conditions are set for $\overline{q}$; the reconstructed mean pressure reads:

$$\begin{aligned} \overline{p}_{BC,free-slip} = \overline{p}_0 + \left\langle\underline{\nabla}\overline{p}\right\rangle_{BC,free-slip} \cdot \left(\underline{x}_{BC} - \underline{x}_0\right), \\ \left\langle\underline{\nabla}\overline{p}\right\rangle_{BC,free-slip} = \left\langle\underline{\nabla}\overline{p}\right\rangle_{REC,0} + \left\{\left[\overline{\rho}_0\left(\underline{g} - \underline{a}_{BC}\right) - \left\langle\underline{\nabla}\overline{p}\right\rangle_{REC,0}\right] \cdot \underline{n}_{wall}\right\}\underline{n}_{wall}, \quad \left.\frac{\partial\overline{q}}{\partial\underline{n}_{wall}}\right|_{wall} = 0 \end{aligned} \tag{4.7}$$

Under no-slip conditions, the in-built motion is imposed along any direction as follows:

$$\begin{aligned} \overline{a}_{wall,F} = a_{wall,S} \Rightarrow \overline{p}_{BC,no-slip} = \overline{p}_0 + \left\langle\underline{\nabla}\overline{p}\right\rangle_{BC,no-slip} \cdot \left(\underline{x}_{BC} - \underline{x}_0\right), \\ \left\langle\underline{\nabla}\overline{p}\right\rangle_{BC,no-slip} = \overline{\rho}_0\left(\underline{g} - \underline{a}_{BC} - \frac{2}{3}\left(\nabla\overline{q}\right)\right), \quad \left.\frac{\partial\overline{q}}{\partial\underline{n}_{wall}}\right|_{SBL} = 0 \end{aligned} \tag{4.8}$$

where the last equality comes from WFs. Under general slip conditions, $\overline{p}_{BC}$ is assumed as a linear combination of the no-slip and free-slip formulae, weighted on the slip coefficient ϕ_s and its complement to the unity. The reconstructed boundary mean pressure and its gradient read:

$$\overline{p}_{BC} = \overline{p}_0 + \left\langle\underline{\nabla}\overline{p}\right\rangle_{BC} \cdot \left(\underline{x}_{BC} - \underline{x}_0\right), \quad \left\langle\underline{\nabla}\overline{p}\right\rangle_{BC} = \phi_s\left\langle\underline{\nabla}\overline{p}\right\rangle_{BC,no-slip} + \left(1 - \phi_s\right)\left\langle\underline{\nabla}\overline{p}\right\rangle_{BC,free-slip} \tag{4.9}$$

Hereafter the reconstructing mean-pressure gradient in (4.7) is formulated. It only involves inner terms '$_{IN}$' to avoid recursion. Under this scope, SPH RANS-CE needs a C_1-consistent SPH filter:

$$\left\langle\underline{\nabla}\overline{p}\right\rangle_{REC,0,CE} = \underline{\underline{B}}_{0,IN}\sum_b\left(\overline{p}_b - \overline{p}_0\right)\underline{\nabla}W_b\omega_b \tag{4.10}$$

where the beta-spline cubic kernel applies. Eq.(4.10) is used in (4.7) to complete the correction stage of RANS-CE and to initialise the surfaces of the solid bodies. It cannot work for SPH RANS-ME for two reasons: it would alter the slip conditions, affecting the inner contribution to the tangential component of the mean-pressure gradient under free-slip conditions; it would introduce some inconsistency as the reconstruction applies before the renormalisation. In SPH RANS-ME, (4.10) is thus replaced by an extrapolation via σ of the temporary C_0-consistent inner term of $\underline{\nabla}\overline{p}$:

$$\left\langle\underline{\nabla}\overline{p}\right\rangle_{REC,0,ME} = \frac{\left\langle\underline{\nabla}\overline{p}\right\rangle_{C0,0,IN}}{\sigma_{0,IN}} = -\frac{\sum_b\left(\overline{p}_b - \overline{p}_0\right)\underline{\nabla}W_b\omega_b}{\sigma_{0,IN}} \tag{4.11}$$

where the cubic anti-cluster kernel substitutes the cubic beta-spline kernel.

4.2. C1-consistent mean TKE and its gradient at fluid-solid interfaces

The spatial reconstruction scheme for the mean TKE and its gradient at fluid-solid interfaces is described hereafter.

The symmetry condition on $\overline{q}$ applies to the fluid-solid interface '$_{wall}$' and approximately also to its neighbourhood. The resulting boundary mean-TKE gradient reads:

$$\left(\underline{\nabla \overline{q}}\right)_{BC} \simeq \left\langle \underline{\nabla \overline{q}} \right\rangle_{REC,0} - \left[\left\langle \underline{\nabla \overline{q}} \right\rangle_{REC,0} \cdot \underline{n}_{wall} \right] \underline{n}_{wall}, \quad \left. \frac{\partial \overline{q}}{\partial \underline{n}_{wall}} \right|_{wall} = 0 \tag{4.12}$$

The reconstructing mean-TKE gradient $\left\langle \underline{\nabla \overline{q}} \right\rangle_{REC,0}$ (m/s^2) is formulated as the analogous quantity for the mean pressure, by replacing $\overline{p}$ with $\overline{q}$ in (4.10) and (4.11). Under no-slip conditions, (4.12) is more accurate because the WF-driven mean-TKE gradient is null all over the NSBL.
The boundary mean TKE for any fluid-body inter-particle interaction reads:

$$\overline{q}_{0s} = \overline{q}_0 + \left(\underline{\nabla \overline{q}}\right)_{0s} \cdot \left(\underline{x}_s - \underline{x}_0\right), \quad \left(\underline{\nabla \overline{q}}\right)_{0s} = \left\langle \underline{\nabla \overline{q}} \right\rangle_{REC,0} - \left[\left\langle \underline{\nabla \overline{q}} \right\rangle_{REC,0} \cdot \underline{n}_{0s} \right] \underline{n}_{0s} \tag{4.13}$$

whereas the boundary mean-TKE for a fluid-wall interaction assumes the following expression:

$$\begin{gathered} \overline{q}_{BC,0w} = \overline{q}_{0w} + \left\langle \underline{\nabla \overline{q}} \right\rangle_{0w} \cdot \left(\underline{x}_{BC} - \underline{x}_0\right), \\ \overline{q}_{0w} = \overline{q}_0, \quad \left(\underline{\nabla \overline{q}}\right)_{0w} = \left\langle \underline{\nabla \overline{q}} \right\rangle_{REC,0} - \left[\left\langle \underline{\nabla \overline{q}} \right\rangle_{REC,0} \cdot \underline{n}_{0w} \right] \underline{n}_{0w} \end{gathered} \tag{4.14}$$

4.3. Emission scheme: numerical mean concentration at the Pollutant Source

Unlike the mesh-based CFD codes for Air Quality (e.g. Efthimiou et al., 2016, [48]), the code of Sec.2 adopts a simpler emission scheme to represent the Pollutant Source, exploiting the Lagrangian approach of the SPH method for sake of efficiency. The emission model for the particle mean concentration at the Pollutant Source PS represents a spatial reconstruction scheme which applies if the following conditions are met: the mean pollutant-mass flow rate at source $\overline{Q}_{PS}$ (kg/s) is known; either the emission mean velocity is assumed uniform or the explicit modelling for jet intrusions in atmosphere is not mandatory. The resulting model an emission scheme under uniform (specific mean) pollutant-mass flow rate. Unless otherwise stated, the PS is hereafter a point or a surface source, and lies within the physical inlet section or slightly downstream, as clarified later.
A physical PS is featured by its input flow rate $\overline{Q}_{PS}$ and area A_{PS} (m^2), and assumes a uniform specific mean pollutant-mass flow rate at source $\overline{\Theta}_{PS}$ (kg/s/m^2). The resulting $\overline{C}$ at PS varies with $\underline{\overline{u}}$ over the local coordinates η (m) and ζ (m) within the plane of the PS. This is assumed normal to the direction of the spatially-averaged mean velocity around the PS. In the discrete, the equivalent '$_{eq}$' numerical source adopts analogous conditions and represents the correct physical flow rate $\overline{Q}_{PS}$ by construction:

$$\begin{gathered} \left\{ \begin{aligned} & \overline{Q}_{PS,eq} = \sum_{iPS=1}^{n_{pPS}} \overline{\Theta}_{PS,eq} \Delta\eta_{iPS} \Delta\zeta_{iPS} \simeq \sum_{iPS=1}^{n_{pPS}} \overline{C}_{iPS} \left(-\underline{n}_{inlet} \cdot \underline{\overline{u}}_{iPS}\right) \Delta\eta_{iPS} \Delta\zeta_{iPS} \\ & \overline{\Theta}_{PS,eq} \quad uniform \Rightarrow \overline{\Theta}_{PS,eq} = \frac{\overline{Q}_{PS,eq}}{A_{PS,eq}}, \quad A_{PS,eq} \equiv \sum_{iPS=1}^{n_{pPS}} \Delta\eta_{iPS} \Delta\zeta_{iPS} \simeq n_{pPS} \left(\Delta x\right)^2_{loc} \end{aligned} \right. \Rightarrow \\ \Rightarrow \overline{C}_{iPS} \simeq \frac{\overline{Q}_{PS}}{\left(-\underline{n}_{inlet} \cdot \underline{\overline{u}}_{iPS}\right) n_{pPS} \left(\Delta x\right)^2_{loc}}, \quad \overline{Q}_{PS,eq} = \overline{Q}_{PS} \end{gathered} \tag{4.15}$$

The subscript '$_{iPS}$' denotes ith position associated with the PS in the 2D time-independent emission pattern of the inlet particles and n_{pPS} is the number of such positions. If no point is detected as internal to the PS volume, the closest position in the pattern is selected. All the particles emitted by the points selected above are called PS inlet particles. It is the inlet particles which cross a PS at some time during their travel. The approximation symbols in (4.15) are due to considering null concentration fluctuations at source. The particle volume is locally assumed uniform and isotropic.
If the PS lies downstream the inlet section, then the following procedures integrate the model above.

The numerical volume of the PS is extruded from the PS 2D surface to the inlet section and cannot overlap with other numerical volumes of PSs. The inlet section is defined to be almost parallel to the plane containing the 2D PS surface. SPH Cm-BE is frozen within the inlet region. Downstream, SPH Cm-BE is frozen if the particle flight time t_{FLY} (s) is smaller than the maximum frozen flight time $t_{FLY,FRO,max}$ (s). This is defined to make the PS particles hold null $\overline{C}$ until reaching the physical PS:

$$t_{FLY,FRO,\max,PS} = \frac{d_{PS,inlet}}{\left|\underline{\overline{u}}\right|_{inlet,\eta_{PS},\zeta_{PS}}}, \quad d_{PS,inlet} = d_{PS,PHY\text{in}let} + L_{inlet}, \quad L_{inlet} = \left[\text{int}\left(4\frac{h}{\Delta x}\right)+1\right]\Delta x + \frac{\Delta x}{2} \tag{4.16}$$

where $t_{FLY,FRO,max}$ depends on the PS. The velocity value in (4.16) is approximated by the corresponding time-dependent value of the first PS position detected by the code in the time-independent pattern of the inlet particles. The distance between the physical PS and the most upstream layer of inlet particles $d_{PS,inlet}$ (m) is the distance between the physical PS and the physical inlet section '$_{PHYinlet}$', increased by the length of the inlet region L_{inlet} (m). This is approximately equal to 4h plus half the particle size. The physical PS has to be close enough to the inlet section to satisfy the following conditions: no other physical PS affects the flow upstream the current PS; the flow locally satisfies Taylor's translation hypothesis for turbulence. The latter considers that the accumulated effect of the stream-wise relative dispersion is negligible and that the mean flow is locally almost 1D. Under these conditions, the local mean velocity at source can be approximately replaced by the inlet mean velocity at the same inlet local coordinates, for the assessments of $\overline{C}_{iPS}$ in (4.15) and $t_{FLY,FRO,max}$ in (4.16). The mean velocity of a PS particle is deemed almost uniform along its trajectory between the numerical inlet section and the physical PS. Any pollutant-mass flux between a computational particle and a neighbouring particle having SPH Cm-BE frozen is inhibited to conserve the pollutant mass. The PS numerical geometry and $t_{FLY,FRO,max}$ are optimise to reduce the distance between the barycentres of the numerical equivalent PS and of the physical PS. A convergence criterion for each distance component is $2\Delta x$. Multiple PSs are treated. Volume PSs are permitted, provided that they belong to the physical inlet section and only extend in the inlet region up to the numerical inlet section. Volume PSs have null $t_{FLY,FRO,max}$. The simulated PSs are stationary. Initial Conditions and the inlet Boundary Conditions can impose additional time-dependent background concentrations.

5. CLOSURE OF THE BALANCE EQUATION FOR THE MEAN CONCENTRATION

The turbulent Schmidt number Sc_T in (2.5) can be alternatively represented by the 'Sc_T-const' approach (Sec.1) or the 'Sc_T-StHIT' model (Sec.5.1), the latter being the default option of the code of Sec.2. Sc_T-StHIT is a closure of the RANS Balance Equation for the mean concentration constrained to Taylor's theory (Taylor, 1922, [17]). It is derived under Stationary and Homogeneous Isotropic Turbulence (HIT), but it approximately applies to non-stationary and inhomogeneous conditions, considering local values for the Lagrangian integral time scale $T_L\left(\underline{x},t\right)$ and for the peak value of the compensated velocity Lagrangian structure function $\tilde{C}_0\left(\underline{x},t\right)$. The effects of velocity autocorrelation, whose role is revised in Fang et al. (2022, [49]), are considered so that the bias of the state-of-the-art deterministic CFD codes in assessing the mean concentration of passive pollutants is inhibited. The application of Sc_T-StHIT closure is expected to be more effective for Lagrangian than Eulerian CFD codes due to the computation of the weighted ensemble mean of the pollutant flight time $\breve{t}_{FP}$ (Sec.5.2). It is the ensemble mean of the pollutant flight time, weighted on the instantaneous pollutant mass per unit of volume. An approximated closed-form solution is derived for $\breve{t}_{FP}$ in Sec.5.2, under RANS-SPH; a variant for Eulerian deterministic RANS CFD codes is also proposed.

5.1. Sc_T-StHIT closure on the turbulent Schmidt number constrained to Taylor's theory

The assumption of a constant Sc_T (Sec.1) is responsible for systematic errors in the $\overline{C}$ field.
A closure on Sc_T is derived to fix this bias above and reproduce the effects of velocity autocorrelation.

Taylor's theory (Taylor, 1922, [17]) quantifies the dispersion tensor $\sigma^2_{x_i^+ x_k^+}$ (m^2), i.e. the ensemble covariance of the displacements of fluid particles emitted by the same point (e.g. a point Pollutant Source PS) in different turbulent realisations of the same fluid flow. The superscript '$^+$' denotes a Lagrangian variable when it can be confused with an Eulerian quantity. Further integration of molecular diffusion, as in Pope (2011, [50]), provided the following overall expression for $\sigma^2_{x_i^+ x_k^+}$:

$$\sigma^2_{x_i^+ x_j^+} = \left\{ 2\sigma^2_{u_i u_j} T_L \left[t_{FLY} - T_L \left(1 - e^{-\frac{t_{FLY}}{T_L}} \right) \right] + 2 D_M t_{FLY} \right\} \delta_{ij} \tag{5.1}$$

where δ_{ij} is Kronecker delta. Eq.(5.1) was derived in the absence of chemical reactions and under HIT, large Re and Taylor's translation hypothesis for turbulence, i.e. $\left(\sigma_u \ll \bar{u}\right)$ with uniform mean velocity. Under these conditions, the following statements apply: fluid particles can be represented by closed numerical particles (at constant C) to assess the mean-concentration field (Pope, 1998, [51]); the flight time t_{FLY} (s) is equal to the weighted ensemble mean of the pollutant flight time (Sec.5.2); the diagonal components of $\sigma^2_{x_i^+ x_k^+}$ are equal to the squares of the mean-plume spreads along the reference axes. The latter suggests constraining Sc_T closure to Taylor's theory (Taylor, 1922, [17]).
Under HIT, the square of the plume spread is isotropic and the velocity components are uncorrelated: $\sigma^2_{x_i^+ x_k^+}$ equals the product of the identity matrix times the average $\sigma^2_{\underline{x}^+}$ (m^2) of the squares of the plume spreads along the reference axes, which can be rearranged as follows:

$$\sigma^2_{\underline{x}^+} \equiv \frac{\sigma^2_{x_k^+}}{3} = \frac{4}{3}\bar{q} T_L \left[t_{FLY} - T_L \left(1 - e^{-\frac{t_{FLY}}{T_L}} \right) \right] + 2 D_M t_{FLY}, \quad \bar{q} = \frac{3}{2}\sigma^2_{u_i} \tag{5.2}$$

where Einstein's summation convention applies to the subscript 'k', the mean TKE is introduced under HIT and the plume spread refers to the relative position of the polluted particles passing for the PS. Following Taylor (1922, [17]) and Pope (2011, [50]), the limit behaviours of (5.2) read:

$$\begin{gathered}
\lim_{t_{FLY} \ll \frac{3D_M}{\bar{q}}} \sigma_{\underline{x}^+} = \sqrt{2 D_M t_{FLY}} \equiv \sigma_{\underline{x}^+, D_M}, \quad \lim_{t_{FLY} \gg \frac{3D_M}{\bar{q}}} \sigma_{\underline{x}^+} = \sqrt{\frac{4}{3}\bar{q} T_L \left[t_{FLY} - T_L \left(1 - e^{-\frac{t_{FLY}}{T_L}} \right) \right]} \equiv \sigma_{\underline{x}^+, T}, \\
\lim_{O\left(\frac{3D_M}{\bar{q}}\right) \approx t_{FLY} \ll T_L} \sigma_{\underline{x}^+} = \sqrt{\frac{2}{3}\bar{q} t^2_{FLY} + 2 D_M t_{FLY}}, \quad \lim_{\frac{3D_M}{\bar{q}} \ll t_{FLY} \ll T_L} \sigma_{\underline{x}^+} = \left(\sqrt{\frac{2}{3}\bar{q}} \right) t_{FLY}, \\
\lim_{t_{FLY} \gg T_L} \sigma_{\underline{x}^+} = \sqrt{2\left(\frac{2}{3}\bar{q} T_L + D_M \right) t_{FLY}}, \quad \lim_{\substack{t_{FLY} \gg T_L \\ \nu_T \gg \frac{9}{8} C_\mu \breve{C}_0 D_M}} \sigma_{\underline{x}^+} = 2\sqrt{\frac{\bar{q} T_L}{3} t_{FLY}},
\end{gathered} \tag{5.3}$$

They are associated with the following regimes, respectively: molecular-diffusion regime; turbulent-dispersion regime 'T'; ballistic & molecular-diffusion regime; ballistic regime; molecular-turbulent-diffusion regime; turbulent-diffusion regime. It was demonstrated that the PDE of (2.5) determines the following expression for the square of the plume spread (e.g. Socolofsky & Jirka, 2002, [52]):

$$\frac{d\sigma^2_{\underline{x}^+}}{dt_{FLY}} = 2\left(K_T\big|_{\underline{x}^+} + D_M\big|_{\underline{x}^+} \right) \tag{5.4}$$

where the average value $\sigma^2_{\underline{x}^+}$ considers isotropic turbulence in the context of 2-equation 1st-order RANS-ME turbulence closures. The a-posteriori correction to K_T is set by equalling the modelled $\sigma^2_{\underline{x}^+}$ in (5.4) to the solution (5.2), and replacing t_{FLY} with the weighted ensemble mean of the pollutant flight time $\breve{t}_{FP}$ (s), defined and motivated in Sec.5.2:

$$K_T = \frac{1}{2}\frac{d\sigma^2_{\underline{x}^+,T}}{d\breve{t}_{FP}} = \begin{cases} \frac{8}{9}\frac{\nu_T}{C_\mu \tilde{C}_0}\left[1-\frac{T_L}{\breve{t}_{FP}}\left(1-e^{-\frac{\breve{t}_{FP}}{T_L}}\right)\right], & \breve{t}_{FP}>0 \\ 0, & \breve{t}_{FP}=0 \end{cases} \tag{5.5}$$

Its limit behaviours are expressed as follows:

$$\lim_{\breve{t}_{FP} \ll T_L} K_T = \frac{\overline{q}\breve{t}_{FP}}{3}, \quad \lim_{\breve{t}_{FP} \gg T_L} K_T = \frac{2}{3}\overline{q}T_L = \frac{8}{9}\frac{\nu_T}{C_\mu \tilde{C}_0} \tag{5.6}$$

The combination of the definition of Sc_T with the first equality of (5.5) provides the Sc_T-StHIT closure to RANS Cm-BE on the turbulent Schmidt number:

$$Sc_{T,k+1} = \frac{\frac{9}{8}C_\mu \tilde{C}_{0,k+1}}{\left[1-\frac{T_{L,k+1}}{\breve{t}_{FP,k+1}}\left(1-e^{-\frac{\breve{t}_{FP,k+1}}{T_{L,k+1}}}\right)\right]}, \quad Sc_T = 2\nu_T\left(\frac{d\sigma^2_{\underline{x}^+,T}}{d\breve{t}_{FP}}\right)^{-1}, \quad Sc_T \equiv \frac{\nu_T}{K_T} \tag{5.7}$$

whose limit behaviours assume the following expressions:

$$\begin{gathered} \lim_{\breve{t}_{FP}\to 0} Sc_T = \infty, \quad \lim_{\breve{t}_{FP} \ll T_L} Sc_T = \frac{3\nu_T}{\overline{q}\breve{t}_{FP}} = 3C_\mu\frac{T_E}{\breve{t}_{FP}} = \frac{9}{4}C_\mu \tilde{C}_0\frac{T_L}{\breve{t}_{FP}}, \\ \lim_{\breve{t}_{FP} \gg T_L} Sc_T = \frac{9}{8}C_\mu \tilde{C}_0 \equiv Sc_{T,\min} \in \left[0;\frac{9}{8}C_\mu C_0 = 0.658\right] \end{gathered} \tag{5.8}$$

The first limit is coded to avoid singularities, the latter to represent the condition $\left[(T_L=0)\cap(\breve{t}_{FP}>0)\right]$. Under HIT and very large flight times, Sc_T tends to $Sc_{T,min}$ that only depends on the turbulence Reynolds number $\mathrm{Re}_T(\underline{x},t)$ via $\tilde{C}_0$, according to Sawford et al. (2008, [53]); further details are given in Amicarelli (2025, [19]). The virtual use of $Sc_T = Sc_{T,min}$ all over the domain would provide a systematic and relevant overestimation of the plume spread at small $\breve{t}_{FP}$:

$$\left.\sigma^2_{\underline{x}^+,T}\right|_{Sc_T=Sc_{T,\min}} = \frac{4}{3}\overline{q}T_L\breve{t}_{FP} \gg \sigma^2_{\underline{x}^+,T} = \frac{2}{3}\overline{q}\left(\breve{t}_{FP}\right)^2, \quad \breve{t}_{FP} \ll T_L \tag{5.9}$$

Under general conditions, the use of any constant value for Sc_T determines a systematic overestimation/underestimation of K_T at small/large $\breve{t}_{FP}$. The PDE of (2.5) closed by Sc_T-StHIT represents the velocity autocorrelation, but it keeps consistent with Fokker-Planck's equation, provided that the spatial variability of the diffusion coefficient of the latter is formally related also to $\frac{\breve{t}_{FP}}{T_L}(\underline{x})$. This ratio only depends on ensemble statistics. Revisiting Fokker-Planck's equation would not change any of its terms, would recover (5.4) with $\left.K_T\right|_{\frac{\breve{t}_{FP}}{T_L}}$ and would obtain (5.5) by comparison with Taylor's theory (Taylor, 1922, [17]). Such alternative demonstration is equivalent to, but longer than the current one. Chemical reactions and molecular diffusion are non-influential, being Sc_T only related to turbulent transport. Sc_T-StHIT does not depend on the shape and size of the PS.

5.2. Weighted ensemble mean of the pollutant flight time for deterministic RANS models

The weighted ensemble mean of the pollutant flight time $\breve{t}_{FP}$ (s) for Sec.5.1 is formulated hereafter. In the present section, any quantity is implicitly considered net of molecular diffusion. Under general conditions, the instantaneous flight time t_{FLY} from Taylor's theory (Taylor, 1922, [17]; Sec.5.1) requires a generalisation as it is not representative any longer of the age of the pollutant and the association between $\sigma^2_{\underline{x}^+}$ and the plume spread (Sec.5.1) would be inaccurate.

The instantaneous pollutant time t_{FP} (s) is first introduced as the average flight time weighted over each fraction of pollutant mass within the fluid particle, at fixed time and space, in a specific virtual realisation of the turbulent flow. This quantity can correctly replace t_{FLY} in Taylor's theory (Taylor, 1922, [17]). Instead, a proper ensemble statistic is requested under deterministic RANS modelling. The ensemble mean $\bar{t}_{FP}$ does not fully represent the pollutant mass associated with $\bar{C}$ because the contributions from each realisation are not weighted over C. This motivates the introduction of the weighted ensemble mean of the pollutant flight time $\overset{C_{D_M=0}}{\breve{t}}_{FP} \equiv \overset{C}{\breve{t}}_{FP} \equiv \breve{t}_{FP}$ (s), whose curved over-bar denotes an ensemble mean weighted on the instantaneous pollutant mass per unit of volume (i.e. C):

$$\breve{t}_{FP} \equiv \frac{\sum_{i=1}^{N_r} t_{FP,i} C_i}{\sum_{i=1}^{N_r} C_i} = \frac{\sum_{i=1}^{N_r} t_{FP,i} C_i}{N_r} \frac{N_r}{\sum_{i=1}^{N_r} C_i} = \frac{\overline{t_{FP} C}}{\bar{C}} \tag{5.10}$$

where N_r is the number of virtual realisations of the same turbulent flow. The quantity $\breve{t}_{FP}$ is an accurate generalisation for t_{FLY}, but (5.10) is associated with two additional BEs for $\overline{t_{FP} C}$ and $\bar{C}$. The latter might be reasonably approximated by Cm-BE, which includes molecular diffusion. Even though the resulting error grows when Re decreases, the role of Sc_T simultaneously diminishes. On the other hand, a new stable scheme for the BE of $\overline{t_{FP} C}$ requires appreciable computational time. Such complication is out of the scope of the current study and would need proper motivation. Instead, a simplified model is adopted, keeping the definition of $\breve{t}_{FP}$, but avoiding the numerical solution of a new PDE. It is assumed that any pollutant turbulent flux of any node with its surrounding environment does not alter the particle $\breve{t}_{FP}$. Under this simplifying hypothesis, $\breve{t}_{FP}$ has the same rate of change of t anywhere and anytime. The simple associated PDE has the following closed-form solution:

$$\left.\frac{d\breve{t}_{FP}}{dt}\right|_{\bar{\underline{u}}_0} = 1 \Rightarrow \breve{t}_{FP,0,k+1} = t_{k+1} - t_{ENT,0} + \breve{t}_{FP,ENT,0} = t_{FLY,0,k+1} + \breve{t}_{FP,ENT,0} \tag{5.11}$$

where the Initial Condition $\breve{t}_{FP,ENT}$ (s) at the particle entry time t_{ENT} (s) is assigned in the following. Under single PS and null background inlet concentration $\bar{C}_{inlet}$, the following expression applies:

$$\breve{t}_{FP,ENT,0} = \begin{cases} \left[\breve{t}_{FP,PS} - \left(t_{FLY,FRO,\max,PS} + \Delta t_{SPPS,PS}\right)\right] \dfrac{\left(-\underline{n}_{inlet} \cdot \left|\bar{\underline{u}}\right|_{\underline{x}_{PS}}\right)}{\left(-\underline{n}_{inlet} \cdot \bar{\underline{u}}_0\right)}, & inlet \\ 0, \quad other \quad BCs/ICs & \end{cases} \tag{5.12}$$

where the first line sets all the SPH inlet particles and the latter is related to the background concentrations for the other subdomains under different BC/IC conditions. $\breve{t}_{FP,PS}$ (s) is the physical input value for $\breve{t}_{FP}$ at the downstream edge of any polluted IC/BC/PS volume: the IC variable $\breve{t}_{FP,ENT}$ is inhomogeneous to reproduce $\left(\breve{t}_{FP} \simeq \breve{t}_{FP,PS}\right)$ when any inlet particle passes the cross-stream section containing the above-mentioned edge. The time lag Δt_{SPPS} is defined in Sec.6.

In the absence of PSs, all the inlet particles are treated with the other BC/IC zones by the second line of (5.12). Its default null value is motivated as follows. The dispersion along the cross-stream directions at the edges of any IC/BC zone is the main concern in terms of plume-spread evolution. Here any plume edge propagates as a point PS as long as $\bar{C}$ is uniform within the IC/BC zone.

Under multiple PSs or $\left(\bar{C}_{inlet} > 0\right)$, several procedures apply. PS inlet particles are associated with a sole PS and (5.12) is approximately adopted. For inlet particles not passing for any PS, a weighted

average is performed involving the null $\breve{t}_{FP,ENT}$ value representative of $\overline{C}_{inlet}$ (with weight equal to 1 or 0 for positive or null $\overline{C}_{inlet}$) and an overall value associated with the set of PSs (with weight equal to the number of PSs). This set value is computed following the first line of (5.12), but introducing a PS-average for each of the following quantities: $\left(t_{FLY,FRO,\max,PS}+\Delta t_{SPPS,PS}\right)$; $\breve{t}_{FP,PS}$; $\underline{\overline{u}}_{PS,inlet}$.
The default null value in (5.12) for the background concentrations in the initial fluid bodies and at the inlet section can be changed in input to possibly improve multiple-PS emission scenarios.
The errors of the current model grows with the distance between the inlet section and the PS section. Such errors also depend on the cross-stream inhomogeneity of the mean velocity. In the presence of an elevated PS, they might contribute to systematically enhance dispersion towards the bottom-wall regions, where mean velocity decreases, with overestimation of $\breve{t}_{FP}$ and underestimation of Sc_T.
Regarding possible uses in Eulerian CFD codes, the PDE associated with (5.11) would read:

$$\frac{\partial \breve{t}_{FP}}{\partial t}=-\overline{u}_j\frac{\partial \breve{t}_{FP}}{\partial x_j}+1 \tag{5.13}$$

where the advection term, implicitly represented by the current Lagrangian code, has to be discretised by a mesh-based method. An alternative formulation for $\breve{t}_{FP}$, conceived for experimental procedures, is reported in Hanna & Britter (2002, [54]) and Bezpalcova (2007, [55]) in terms of 'travelling time', as function of the 'effective transport speed' (or 'cloud advection speed').

6. SUB-PARTICLE POLLUTANT-SOURCE (SPPS) SCHEME

The size of the numerical Pollutant Source PS can be conveniently set larger than the physical PS, but this difference causes a spurious numerical diffusion at PS. To minimise such diffusion, the following Sub-Particle Pollutant-Source (SPPS) spatial reconstruction scheme is introduced. It manages the very early stage of the plume development within the particles which discretise the PS. Based on experimental evidence, the intrusion model reported in Cushman-Roisin (2019, [56]) for a turbulent jet in a still environment expresses the radius of the 'jet-environment' intrusion region R_x (m) as function of the stream-wise distance from the emission section of the jet (i.e. the PS section):

$$R_x=\frac{\left(x-x_{PS}\right)}{5}+R_{PS};\quad R_x\equiv 2\sigma_z=2\sigma_y;\quad R_{PS}=\begin{cases}\sqrt{\dfrac{A_{PS}}{\pi}}, & 3D\\ \dfrac{A_{PS}}{2W_{PS}}, \quad W_{PS}\equiv 1, & 2D\end{cases} \tag{6.1}$$

where molecular diffusion is neglected. The x-axis is here aligned with the average mean velocity at the PS. R_x is measured as the mean-plume radius, being the jet polluted by a passive scalar. R_{PS} (m) is the radius of the isotropic equivalent physical PS; it is the radius of the circle in 3D (or the half-length of the segment in 2D) which has the same area A_{PS} (m^2) as the physical PS. Eq.(6.1) is also valid for any velocity deviation of the jet with respect to a uniform, non-null environment mean velocity U_{env} (m/s), being U_{emi} (m/s) the average mean velocity at the exit of the emission duct ($x=x_{PS}$). The numerical '$_{num}$' PS discretises the physical PS using n_{pPS} numerical points (Sec.4.3). The area and radius of the numerical PS are expressed as follows:

$$A_{PS,num}=\begin{cases}\pi R_{PS,num}^2=\left(\Delta x\right)^2 n_{pPS}, & 3D\\ 2R_{PS,num}W_{PS}=n_{pPS}\left(\Delta x\right)W_{PS}, & 2D\end{cases}\Rightarrow R_{PS,num}=c_{SPPS}\left(\Delta x\right);\quad c_{SPPS}\equiv\begin{cases}\sqrt{\dfrac{n_{pPS}}{\pi}}, & 3D\\ \dfrac{n_{pPS}}{2}, & 2D\end{cases} \tag{6.2}$$

In terms of equivalent radius, the numerical PS of (6.2) matches the downstream evolution of the isotropic equivalent physical PS of (6.1) at a specific position noticed as x_{SPPS} (m):

$$R_{x_{SPPS}}=R_{PS,num}\Rightarrow\left(x_{SPPS}-x_{PS}\right)=\max\left\{5\left(c_{SPPS}\Delta x-R_{PS}\right);0\right\} \tag{6.3}$$

where a null limiter is integrated to avoid upstream unphysical dispersion. The SPPS scheme applies to the SPPS region, which is the space contained by the extrusion of the numerical PS downstream the position of the physical PS to $\underline{x}_{SPPS}$. In this region, all the pollutant fluxes of a PS particle are zeroed, including the opposite fluxes of the neighbouring particles. For each PS, a uniform SPPS frozen time lag Δt_{SPPS} (s) is assessed as follows:

$$\Delta t_{SPPS} \equiv t_{FLY,SPPS} - t_{FLY,PS} \simeq \frac{\left(x_{SPPS} - x_{PS}\right)}{\left|\overline{u}\right|_{\underline{x}_{PS}}} \tag{6.4}$$

The SPPS scheme freezes the mean plume downstream the PS up to a maximum length of few SPH particle sizes. The SPPS scheme is thus interpreted as a spatial reconstruction scheme. It is consistent, being non-influential for $\Delta x \rightarrow 0$. The SPPS scheme effectively inhibits numerical diffusion at PS also because no spatial filter applies. The residual part of the $\overline{C}$ numerical diffusion decreases with the flight time from the PS to the SPPS downstream edge. Here the residual errors are mainly related to representing a uniform $\overline{C}$ field within a PS particle. Compared to the ballistic regime of Taylor's theory (Taylor, 1922, [17]) in (5.3), the jet-intrusion model has the advantage of being valid for any velocity deviation of the jet, but it is more approximated under null U_{emi}, which features the ballistic regime. The two approaches are equivalent if the following conditions are all satisfied: U_{env} and U_{emi} are uniform; $R_{PS} << \Delta x$; $\sigma_w = \frac{\left|\overline{u}\right|}{10}$, being σ_w (m/s) the standard deviation of the vertical velocity.

7. EXPERIMENTAL TURBULENT SHEAR FLOW WITH ELEVATED POLLUTANT SOURCE

The new features of the code of Sec.2 are validated on the experimental turbulent shear flow of Fackrell & Robins (1982, [8]) with an Elevated Pollutant Source (EPS). Full description of the test case is available in Amicarelli (2024, [18]), where the previous code version was tested. This benchmark is associated with an application to Outdoor Air Quality with a stack ordinary emission of propane (C_3H_8) at the scale ratio of 1:1000. The SPH particle size is Δx=0.03 m. The reference simulation adopts the Sc_T-StHIT closure and the SPPS scheme. The latter is deactivated in the two simulations which exclusively focus on the differences between Sc_T-StHIT and Sc_T-const approaches, also comparing with the measurements of Fackrell & Robins (1982, [8]), and with the LSM-FDM numerical results of Amicarelli et al. (2011, [20]). For sake of simplicity, jet intrusion at PS is not explicitly modelled. The $\overline{C}$ field around the most upstream monitoring point of the horizontal profile is almost discontinuous requiring the nearest-particle method (Sec.3.8).

Figure 1 shows the $\overline{C}$ horizontal profile of the maxima along the vertical and synthesises the overall validation of the Sc_T-StHIT closure on the present benchmark. In this scope, the Sc_T-const approach was found to systematically and progressively underestimate $\overline{C}$ close enough to the PS (Amicarelli, 2024, [18]). The turbulence closure Sc_T-StHIT permits to fix this bias (Figure 1) because it is constrained to Taylor's theory (Taylor, 1922, [17]) and indirectly represents the velocity autocorrelation (Sec.5). The benefits provided by the Sc_T-StHIT closure are highlighted by comparison with the measurements of Fackrell & Robins (1982, [8]) showing larger improvements closer to the PS, up to one order of magnitude. The turbulence closure Sc_T-StHIT seems to fill the gap between the Sc_T-const approach, representative of deterministic RANS CFD (no matter about the numerical method), and the simulation of Amicarelli et al. (2011, [20]), representative of stochastic RANS CFD in simulating the dispersion of a passive pollutant in a turbulent shear flow.

The benefits given by Sc_T-StHIT closure are confirmed by the vertical profiles of relative $\overline{C}$ normalised over the local maximum along the vertical (Figure 2). Despite some residual overestimations at ground, close enough to the PS, the overall improvements are systematic, especially for the three most upstream profiles, where the Sc_T-StHIT results are much closer to the available measurements (Fackrell & Robins, 1982, [8]) than using the Sc_T-const approach.

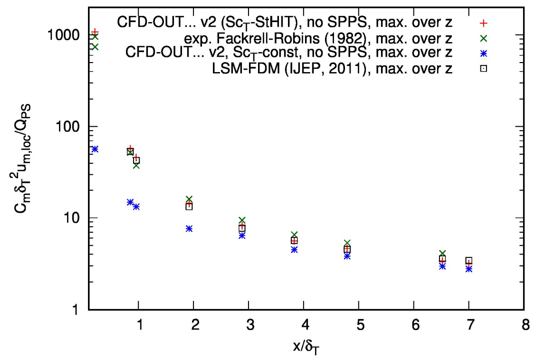

Figure 1. Shear flow with EPS: $\overline{C}$ horizontal profile (t=t_f, y=y_{PS}=0). Validation and inter-comparisons on the maxima along the vertical: CFD-OUT-sweePDF v.2.0.0, Sc_T-StHIT, SPPS off (+); experimental values (Fackrell & Robins, 1982, [8]: ×); sparring simulation with Sc_T-const approach, SPPS off (*); LSM-FDM numerical results of Amicarelli et al. (2011, [20]; □).

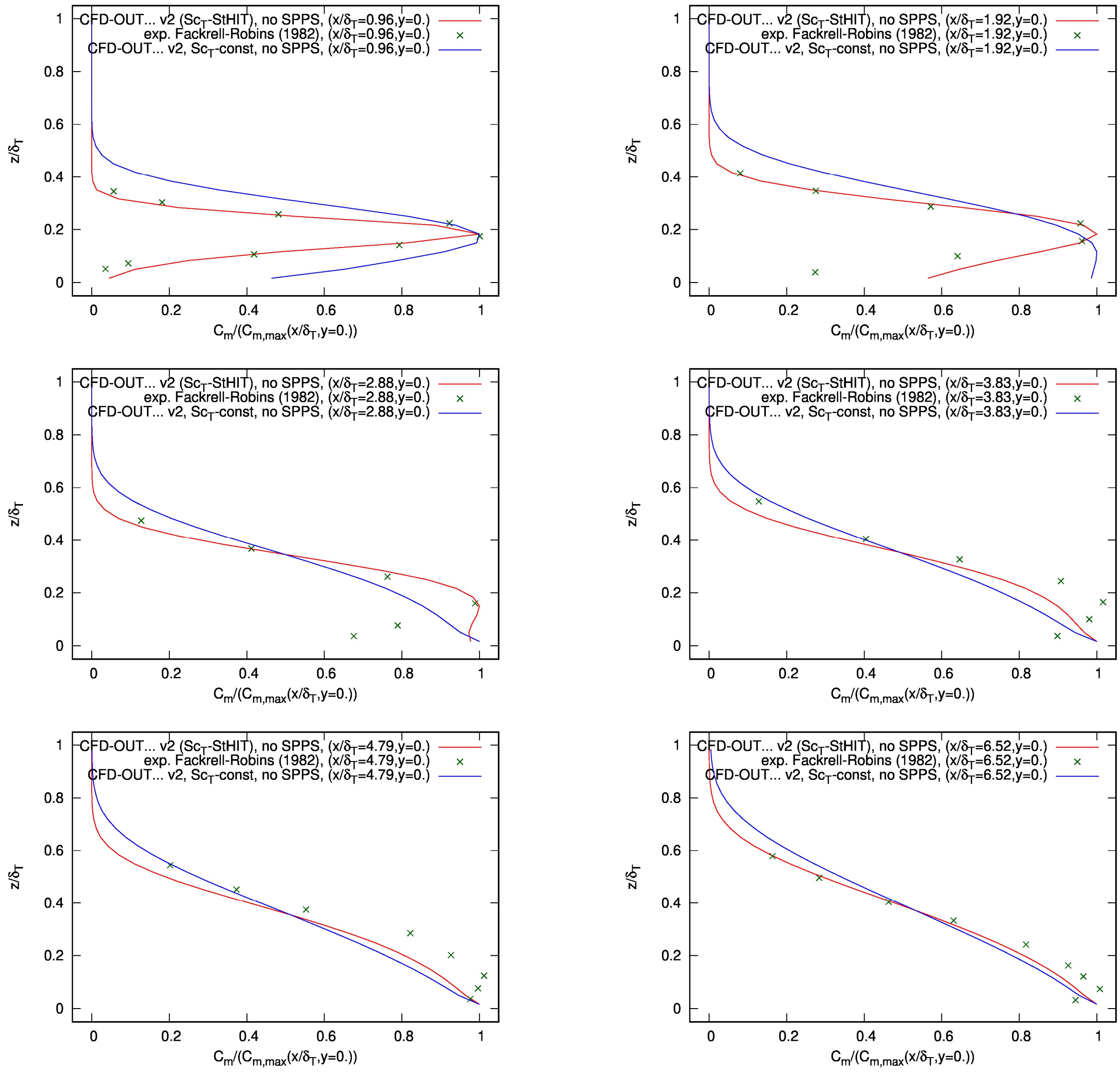

Figure 2. Shear flow with EPS: vertical profiles of relative dispersion (t=t_f, y=y_{PS}). From top-left to bottom-right panels: x/δ_T=0.96, 1.92, 2.88, 3.83, 4.79, 6.52. CFD-OUT-sweePDF v.2.0.0, Sc_T-StHIT, SPPS off (—); experimental values (Fackrell & Robins, 1982, [8]: ×); sparring simulation with Sc_T-const approach and SPPS off (—).

The SPPS scheme is finally activated to configure the reference simulation of the code of Sec.2 for the current test case, keeping the Sc_T-StHIT closure on (Figure 3). The resulting horizontal profiles of $\overline{C}$ are point-to-point compared with the available measurements (Fackrell & Robins, 1982, [8]) also at the ground level (Figure 3, left panel). The numerical results correctly match the measured values with limited errors. They refer to an anticipated arrival of the mean plume at ground with a coherent anticipation of $\overline{C}$ peak at the same height. The simulated $\overline{C}$ is limitedly overestimated at $x<\delta_T$ and slightly underestimated at $x>\delta_T$. The incremental contribution of the SPPS scheme is secondary and slightly deteriorates the quantitative performance of the code (Figure 3, right panel). Beyond this minor drawback, possibly due to some counterbalancing effect with the SPH truncation errors, SPPS provides a more reliable physical description of the plume around the PS and is kept active in the following validations which motivate its use.

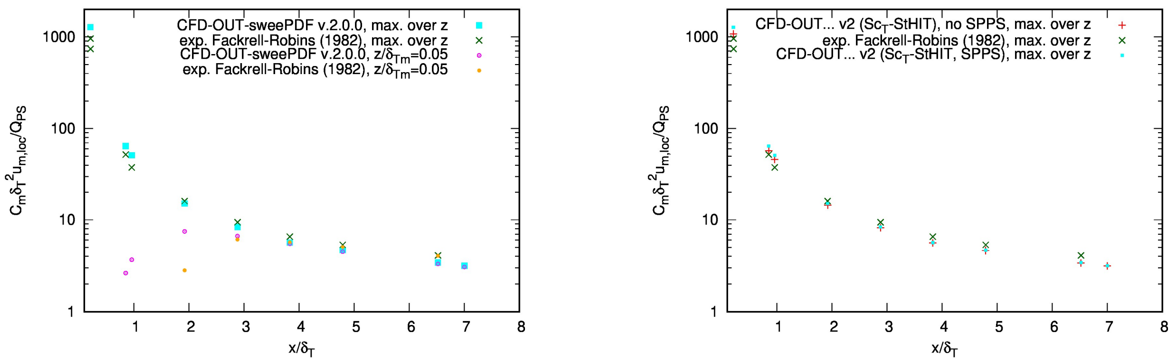

Figure 3. Shear flow with EPS: $\overline{C}$ horizontal profiles (t=t_f, y=y_{PS}). Left panel: validation on the maxima along the vertical and on the ground-level values. Right panel: inter-comparisons on the maxima with/without SPPS. CFD-OUT-sweePDF v.2.0.0 (reference simulation, i.e. Sc_T-StHIT and SPPS on: ■, ○); experimental values (Fackrell & Robins, 1982, [8]: ×, ●); CFD-OUT-sweePDF v.2.0.0 with Sc_T-StHIT and SPPS off (+).

The benefits of the Sc_T-StHIT closure vs. the Sc_T-const approach are also analysed in terms of $\overline{C}$ field and plume shape. The comparison of the vertical section of $\overline{C}$ field passing for the PS (Figure 4) shows that the upper and lower edges of the Sc_T-StHIT plume depict a linear shape close enough to the PS, coherently with Taylor's theory (Taylor, 1922, [17]) and contrarily to the parabolic shape that the Sc_T-const plume reproduces all over the domain. This is due to the absence of velocity autocorrelation. Sc_T-StHIT relevantly reduces the turbulent dispersion assessed by Sc_T-const: the plume depth is smaller; its $\overline{C}$ maxima along the vertical are larger. The SPPS scheme qualitatively adds a secondary improvement to the plume shape very close to the PS by freezing $\overline{C}$ for a distance of 2.11Δx to permit the small physical plume to correctly reach the particle size. SPPS effect in the non-frozen region is a translation of $\overline{C}$ field downstream.

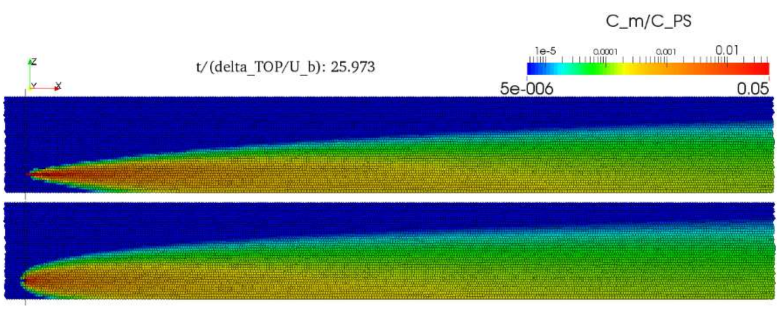

Figure 4. Shear flow with EPS. Vertical slice (y=y_{PS}) of the non-dimensional field for $\overline{C}$ (t=ca.t_f). Top panel: Sc_T-StHIT closure (and SPPS on). Bottom panel: Sc_T-const approach (and SPPS off). The vertical line represents the vertical section containing the PS.

Analogous improvements are found in the representation of the horizontal turbulent fluxes of the pollutant. The plume width is also correctly reproduced by Sc_T-StHIT with a reduced dispersion close enough to the PS where the plume width shows a linear growth (Figure 5). Due to the optimised positions of the lateral boundaries, the over-diffusive reproduction of the plume width by Sc_T-const also triggers some side effects which might reach the monitors along the domain central section.

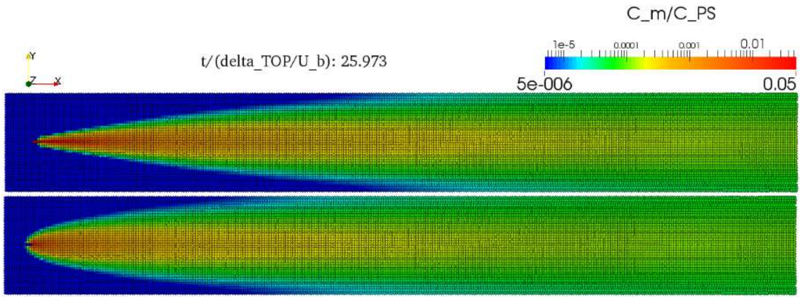

Figure 5. Shear flow with EPS: non-dimensional field for $\overline{C}$ (t=ca.t_f). Horizontal slice (z=z_{PS}). Top panel: Sc_T-StHIT closure (and SPPS on). Bottom panel: Sc_T-const approach (and SPPS off).

The iso-surfaces of the non-dimensional $\overline{C}$ are obtained from the grid points (Figure 6) and represents a 3D layout of the $\overline{C}$ field. The Sc_T-StHIT iso-surfaces of the largest values involve bigger volumes and reaches longer stream-wise distances than Sc_T-const, due to the proper amount of turbulent dispersion. The iso-surface of the lowest value shows the correction to the plume shape.

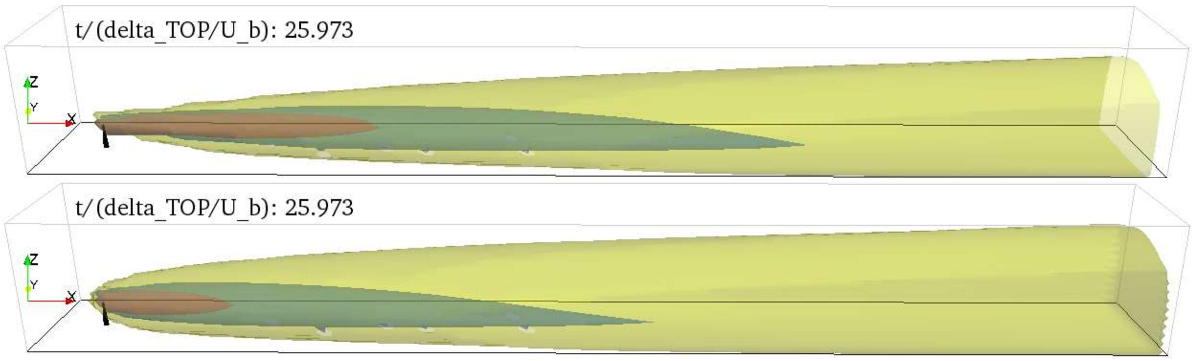

Figure 6. Shear flow with EPS: iso-surfaces of $\overline{C}$ normalised by its maximum value at PS (red: 5×10^{-4}, cyan: 2×10^{-4}, yellow: 1×10^{-5}) at t=ca.t_f. Top panel: Sc_T-StHIT closure (and SPPS on). Bottom panel: Sc_T-const approach (SPPS off).

Sc_T-StHIT introduces the estimations of $\breve{t}_{FP}$ and Sc_T. The central vertical slice of the field of the ratio $\breve{t}_{FP}/T_L$ (Figure 7, top panel) represents the growth of the weighted ensemble mean of the pollutant flight time with the distance from the PS and its decrease with height due to larger values of the mean velocity, associated with smaller flight times. This dependency on z is amplified by T_L increase with height. Almost the whole domain is interested by a hybrid regime of pollutant transport, whereas the pure ballistic regime ($\breve{t}_{FP}/T_L\leq0.05$) can be detected close to the PS. The spatial pattern of $\breve{t}_{FP}/T_L$ rules the Sc_T field (Figure 7, bottom panel), whose vertical inhomogeneity is amplified by Re_T via $\tilde{C}_0$ (Sec.5.1). The value of Sc_T=0.72 (Sec.5), associated with Sc_T-const approach, represents an intermediate Sc_T value in the downstream half of the domain, where $\overline{C}$ differences with respect to Sc_T-StHIT are more limited. Sc_T ranges from ca.0.3 to over 100. Its assessment is suspended in the Cm-BE frozen region (Sec.4.3), which includes the SPPS region (Sec.7).

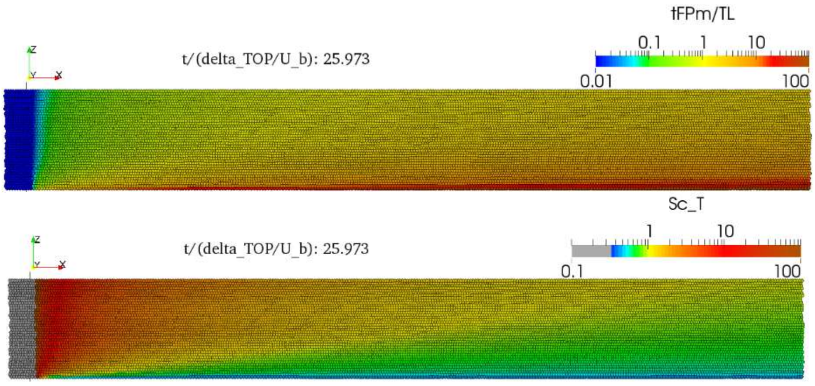

Figure 7. Shear flow with EPS: vertical slices (y=y_{PS}) of the fields of $\breve{t}_{FP}/T_L$ (top panel) and Sc_T (bottom panel) at t=ca.t_f. CFD-OUT-sweePDF v.2.0.0: reference simulation (Sc_T-StHIT closure and SPPS on).

Thanks to the Sc_T-StHIT closure, the residual errors of the reference simulation are limited; their possible sources are discussed in the following. The approximated model for $\breve{t}_{FP}$ (Sec.5.2) might enhance turbulent dispersion towards the wall where the mean velocity decreases and ScT is probably underestimated. In the wall SPH neighbourhood, along the mean plume centreline, the same bias might play a secondary beneficial role counterbalancing the under-diffusive effect induced by the C_0-consistent BC terms in SPH Cm-BE. The SPH truncation error in reproducing a quasi-Laplacian might also play an appreciable role far from the wall if $\overline{C}$ is strongly non-linear. The computational cost of the reference simulation is quantified by the Total Virtual Memory *TVM*=5.77GB and the elapsed time t_{ela}=9h33min40s on 3.5 physical cores (with hyper-threading) of an i9-13900HX CPU processor. The very small number of cores is only due to a very-low-cost operative strategy.

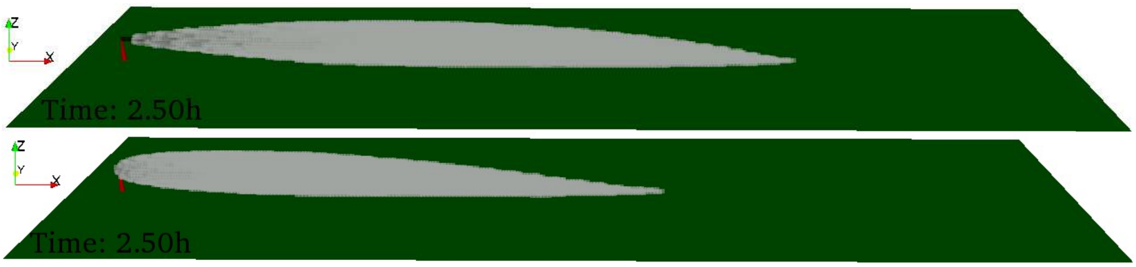

Figure 8. Shear flow with EPS: $\overline{C}$ field (t=t_f). Stack ordinary emission of C_3H_8 (full-scale application) with $\overline{C}$ going from transparent white (null values) to black saturated at PS (stack in red, grassy flat topography in green). Top panel: Sc_T-StHIT closure (and SPPS on). Bottom panel: Sc_T-const approach (and SPPS off).

The present test case is associated with an application to Outdoor Air Quality with a stack ordinary emission of hydrocarbons (C_3H_8) over flat topography. At full scale, the improvements given by Sc_T-StHIT (vs. Sc_T-const) and by the SPPS scheme (vs. an implicit numerical diffusion at source) are appreciated in the 3D representation with progressive colouring of Figure 8, where the most polluted region of the air-flow is highlighted. The concentration freezing is clearly visible just downstream the PS as well as the ballistic regime with linear growth of the plume spread in the early stages of the pollutant transport. Under the reference simulation, the stream-wise length of the most polluted region is longer than the sparring simulation with Sc_T-const and the plume spread is smaller near the PS.

8. CONFINED FLOW PAST A WALL-MOUNTED CUBIC OBSTACLE WITH CANYON POLLUTANT SOURCE

The code of Sec.2 is validated on a confined flow past a wall-mounted cubic obstacle of size H_b (m) with a canyon Pollutant Source. It is the reproduction of the experimental air-flow of Martinuzzi & Tropea (1993, [57]) combined with the dispersion scenario whose BCs are set as close as possible to the experiment of Mavroidis et al. (2003, [58]). The full description of the test case is available in

Amicarelli (2024, [18]), where the previous code version was tested. The non-dimensional concentration $\pi_{\overline{C}}$ is defined according to Mavroidis et al. (2003, [58]). The test case is associated with an application to Indoor Air Quality with an accidental release of hydrocarbons (C_3H_8) from a pipeline in a ventilated indoor parking lot with guard post (scale ratio 1:100). The reference simulation is compared with the results of the previous version of the code (Amicarelli (2024, [18]), featured by the Sc_T-const approach and the absence of the SPPS scheme.

In the horizontal slice of the $\overline{C}$ field passing for the obstacle barycentre (Figure 9), the Sc_T-StHIT closure improves the plume representation upstream the obstacle. Here the plume is much narrower than using the Sc_T-const approach, evolves with a linear growth coherently with Taylor's theory (Taylor, 1922, [17]) and is more influenced by the displacement zone of the air-flow, induced by the presence of the obstacle. Downstream, the $\overline{C}$ field does not show relevant differences among the two approaches. In the non-frozen region of the reference simulation, the SPPS scheme simply translates the mean plume downstream of $2.40\Delta x$, which is the length of the SPPS region.

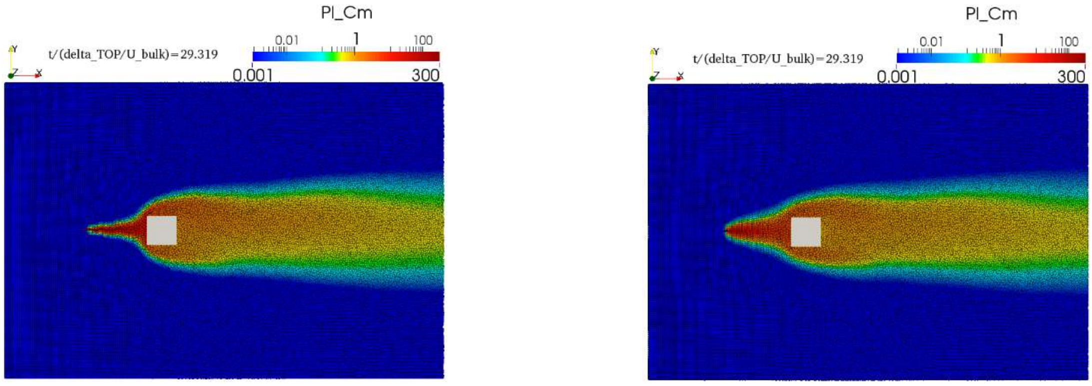

Figure 9. Confined flow past a cube with CPS at t=ca.t_f. Non-dimensional field of $\pi_{\overline{C}}$ (horizontal slices, z=H_b/2). Left panel: reference simulation (Sc_T-StHIT; SPPS on). Right panel: simulation with Sc_T-const (Amicarelli, 2024, [18]).

Analogous Sc_T-StHIT improvements are recorded over the vertical slice of Figure 10, where the further confinement exerted by the bottom wall is more influential with the Sc_T-const approach; this also shows some extra dispersion around the PS, where its underestimation of Sc_T is maximum.

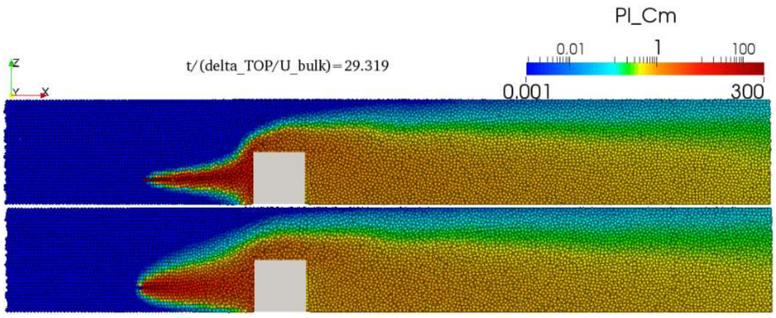

Figure 10. Confined flow past a wall-mounted cube with CPS. Vertical slices (y/H_b=y_{PS}/H_b=0) of the field of $\pi_{\overline{C}}$. Top panel: reference simulation (Sc_T-StHIT). Bottom panel: simulation with Sc_T-const (Amicarelli, 2024, [18]).

The Sc_T field depends on $\breve{t}_{FP}/T_L$ and Re_T (or ν_T for sake of simplicity). The Lagrangian integral time scale T_L grows with the distance from any wall and decreases with larger Re_T, which occurs in the side recirculation regions, the cavity and the wake (Figure 11, top panel).

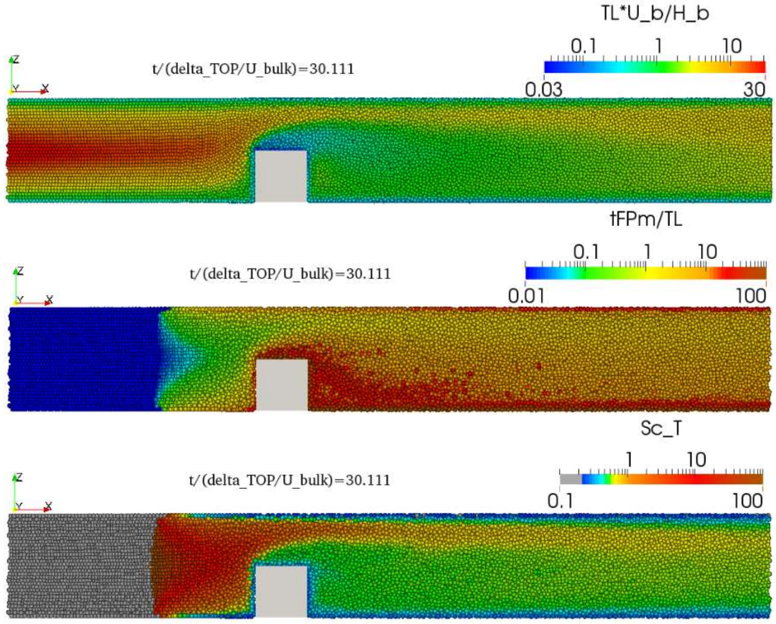

Figure 11. Confined flow past a cube with CPS. Reference simulation (Sc_T-StHIT): vertical slices (y/H_b=0) of the fields of $T_L U_b/H_b$ (top panel), $\breve{t}_{FP}/T_L$ (centre panel) and Sc_T (bottom panel) at t=t_f.

In this reference section, T_L varies between zero (on the walls) to its maximum value at the core of the incoming flow where it is equal to ca.30 times the period necessary to make the fluid cover a cube face at the bulk velocity U_b (m/s), i.e. the average inlet mean velocity. The ratio $\breve{t}_{FP}/T_L$ grows with the stream-wise distance and towards any wall due to larger t_{FLY} and smaller T_L values (Figure 11, centre panel). A relevant area of local maxima is shown in the recirculation regions where both the fluid particles and the SPH control volumes are entrapped for some flight time. This makes the lower half of the domain be featured by longer $\breve{t}_{FP}$ values, also due to the speedup induced by the abrupt shrinkage in the upper half. These behaviours are amplified by the spatial pattern of T_L, except for the cavity core. The pure ballistic regime of pollutant transport (Sec.5.1) covers a small region close to the PS, whereas the turbulent-diffusion regime ($\breve{t}_{FP}/T_L \geq 20$) rules the recirculation regions and the SPH particles close to the downstream walls. The Sc_T field (Figure 11, bottom panel) strongly depends on $\breve{t}_{FP}/T_L$, except for the cavity core due to the counterbalancing effect of a maximum area of Re_T. The value of Sc_T=0.72 (Sc_T-const approach, Sec.1) is representative of a very limited volume, mainly in the upper half of the domain, downstream the shrinkage. This makes Sc_T-StHIT induce relevant Sc_T reductions upstream the obstacle and appreciable Sc_T increases in the cavity and wake regions. It explains why the validation of the mean concentration, which only occurs in the cavity and the wake, is not practically affected by the improvements to Sc_T, contrarily to the assessment of the plume evolution upstream the obstacle. Sc_T globally ranges from ca.0.2 at the top wall to over 100 in the core of the cross-stream section containing the PS.

The integrated application of the spatial reconstruction schemes for the mean pressure and the mean TKE (Sec.4), the C_1-consistent SPH quadrature formulae (Sec.3), several stabilisation strategies (Amicarelli, 2024, [18]) and the SPH-TSE filter (Amicarelli, 2025, [19]) at the grid points permits to reproduce a regular field of the non-dimensional mean pressure (Figure 12). The horizontal slice of the mean reduced-pressure coefficient $\pi_{\bar{p}_r}$ passing for the obstacle barycentre shows the upstream stagnation area, the depression volumes in the side recirculation regions and a downstream area of local maxima along the domain centreline where the downward flow interacts with the bottom wall.

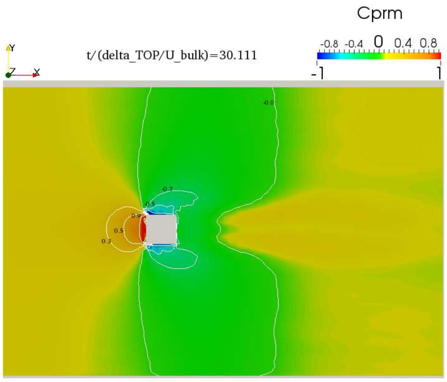

Figure 12. Confined flow past a cube with CPS. Horizontal slice (z=H_b/2) of the mean reduced-pressure coefficient $\pi_{\bar{p}_r}$ at t=t_f; iso-lines (-0.5, -0.3, 0, 0.3, 0.5, 0.9) from grid points. Reference simulation.

The combined application of the spatial reconstruction scheme for the mean TKE (Sec.4.2), the C_1-consistent SPH quadrature formulae (Sec.3), several stabilisation strategies (Amicarelli, 2024, [18]) and the RANS Wall Functions (Amicarelli, 2024, [18]) allows the code to reproduce an accurate field of $\bar{q}$, as demonstrated by the quantitative validations in Amicarelli (2024, [18]). Here a further qualitative demonstration is given by the cross-stream vertical slice containing the trailing edge (Figure 13) where the regular field of the mean TKE shows an arch of maxima in the side recirculation regions. This pattern of $\bar{q}$ peaks matches the upper bound of the experimental arch vortex described in Martinuzzi & Tropea (1993, [57]) just downstream the trailing edge.

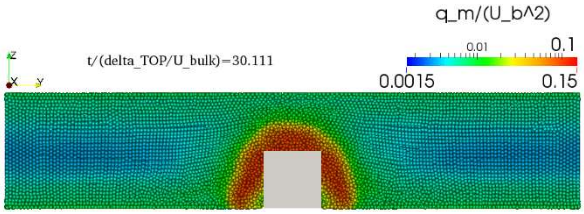

Figure 13. Confined flow past a cube with CPS. Cross-stream vertical slice containing the trailing edge (x=H_b) of the non-dimensional $\bar{q}$ at t=t_f. Reference simulation.

The computational cost of the reference simulation is quantified by TVM=15.1GB and t_{ela}=ca.16h25min on 3.5 physical cores (with hyper-threading) of an i9-13900HX CPU processor. Compared to the simulation with Sc_T-const approach (Amicarelli, 2024, [18]), the elapsed time t_{ela} of the reference simulation with the Sc_T-StHIT closure shows an increase of 3% as all the new quantities are computed on the fly to minimise TVM. The very small number of cores is only due to a very-low-cost operative strategy; about massively-parallelised SPH runs, one might refer to Cui et al. (2020, [59]) results of 1024-core SPH simulations on the impingement and solidification of Super-cooled Large Droplets on aircraft surfaces.

9. CONCLUSIONS

The turbulent Schmidt number Sc_T is systematically assumed constant ('Sc_T-const approach') by deterministic RANS CFD codes. This is equivalent to neglecting velocity autocorrelation and setting Sc_T to an intermediate value all over the domain. Under the best conditions, the chosen constant is test-case independent. Despite being a state-of-the-art practise, the adoption of any constant Sc_T value determines a systematic overestimation/underestimation of the turbulent dispersion coefficient K_T at small/large flight times since the Pollutant Source PS. To overcome this limit, the model Sc_T-StHIT is presented and validated. It is a turbulence closure on Sc_T of the RANS Balance Equation for the mean concentration $\bar{C}$ constrained to Taylor's theory (Taylor, 1922, [17]). It is derived under

Stationary and Homogeneous Isotropic Turbulence (HIT), but approximately applies to non-stationary and inhomogeneous conditions, considering local values for the Lagrangian integral time scale $T_L\left(\underline{x},t\right)$ and for the peak value of the compensated velocity Lagrangian structure function $\tilde{C}_0\left(\underline{x},t\right)$. The effects of velocity autocorrelation are reproduced. Sc_T-StHIT is written as the default Sc_T approach of CFD-OUT-sweePDF v.2.0.0 (Amicarelli et al.). It is a Lagrangian deterministic RANS CFD-SPH code for turbulent flows with pollutant dispersion under stationary and non-stationary regimes. Thanks to Sc_T-StHIT, Sc_T has a hyperbolic behaviour close to the Pollutant Source PS; under large flight times Sc_T tends to a minimum that only depends on the local value of the turbulence Reynolds number Re_T. Sc_T-StHIT formulation applies to any number/shape/size of PSs and any BC/IC for $\overline{C}$. The mathematical and numerical models of Sc_T-StHIT are proposed for both Lagrangian and Eulerian deterministic RANS CFD codes. However its application might be more effective for Lagrangian codes due to the computation of the weighted ensemble mean of the pollutant flight time $\breve{t}_{FP}$.

Sc_T-StHIT validations concern two test cases and comparisons with the available measurements (Fackrell & Robins, 1982, [8]), the numerical results of a stochastic RANS-LSM model (Amicarelli et al., 2011, [20]) and the previous version of the aforementioned code using the Sc_T-const approach (Amicarelli, 2024, [18]). These incremental validations involve an experimental turbulent shear flow with elevated PS and a confined turbulent flow past a wall-mounted cubic obstacle with Canyon PS. These benchmarks are associated with full scale applications to Outdoor/Indoor Air Quality.

The mean concentration assessed with the RANS CFD-SPH code using the Sc_T-StHIT closure is close to the experimental values. Sc_T-StHIT relevantly reduces the turbulent dispersion overestimated by Sc_T-const approach near the PS, with $\overline{C}$ improvements up to one order of magnitude. Sc_T-StHIT fills the most gap between deterministic RANS CFD (no matter about the numerical method), featured by the Sc_T-const approach, and stochastic RANS CFD in simulating the dispersion of a passive pollutant in a turbulent shear flow, provided the same accuracy level for the velocity statistics. Sc_T-StHIT makes the plume depict a linear shape in the ballistic regime of turbulent transport near the PS, coherently with Taylor's theory (Taylor, 1922, [17]) and contrarily to the parabolic shape that the Sc_T-const plume reproduces all over the domain.

The Sc_T field depends on the ratio $\breve{t}_{FP}/T_L$ and Re_T (or ν_T for sake of simplicity). All these quantities are estimated by the code. T_L grows with the distance from any wall (showing a near-wall linear behaviour) and decreases with larger Re_T, which occurs in the side recirculation regions, the cavity and the wake zones around the obstacle. The ratio $\breve{t}_{FP}/T_L$ grows with the stream-wise distance and also towards any wall due to larger t_{FLY} and smaller T_L values; local maxima are shown in the recirculation regions where both the fluid particles and the SPH control volumes are entrapped for some flight time. The ballistic regime of pollutant transport $\left(\breve{t}_{FP} \le ca.0.05T_L\right)$ is detected close to the PS, whereas the turbulent-diffusion regime $\left(\breve{t}_{FP} \ge ca.20T_L\right)$ rules the recirculation regions and the most downstream zones, especially close to walls. The Sc_T field strongly depends on $\breve{t}_{FP}/T_L$, except for the cavity core due to the counterbalancing effect of Re_T. The discrete values of Sc_T globally ranges from ca.0.2 to over 100 at the core of the cross-stream section containing the PS.

A turbulent closure on Sc_T for the mean concentration constrained to Taylor's theory (Taylor, 1922, [17]) seems a novelty in CFD as well as any computation of Sc_T. The assessment of T_L is an original contribution of the current code in the scope of deterministic CFD since Amicarelli (2024, [18]). The computation of $\breve{t}_{FP}$ represents an original feature of the current study.

The Sc_T-const approach was sometimes used for data-assimilation or calibration purposes as a diagnostic strategy and/or to compensate some numerical bias (e.g., in the estimation of the mean TKE). Analogously, the Sc_T-StHIT closure might be multiplied by an explicit calibration/assimilation factor within the same scope, keeping a better accuracy.

The turbulence closure Sc_T-StHIT might also interest RANS-SPDF (Scalar PDF) models (Haworth, 2010, [60]), a category of stochastic RANS CFD codes not reproducing the velocity autocorrelation. Sc_T-StHIT could constrain the Sub-Grid-Scale (SGS) turbulent Schmidt number $Sc_{T,\Delta}$ used in some LES models as in Meringolo et al. (2024, [61]). This represents one of the rare LES SPH studies on pollutant transport with explicit turbulent transport term, giving a physically-based value to the SGS coefficient of turbulent dispersion. That study assumed $Sc_{T,\Delta}$=0.70, focused on water quality, considered an active pollutant (i.e. buoyancy effects were simulated) and provided a quantitative validation on the LES-filtered concentration in 2D. Sc_T-StHIT might apply to the turbulent Prandtl number for the diffusion of the mean temperature.

A separate validation involves the Sub-Particle Pollutant Source (SPPS) scheme. It is a new 'sub-grid' spatial reconstruction scheme for $\overline{C}$ working in a very limited region just downstream the PS. SPPS allows to set the size of the numerical PS conveniently larger than the physical PS, minimising any spurious numerical diffusion at PS. It is constrained to the model of Cushman-Roisin (2019, [56]) for the intrusion of a turbulent jet in a still environment. SPPS freezes $\overline{C}$ for a distance of very few particle sizes from the PS to permit the small physical plume to correctly reach the particle size. The use of a sub-grid scheme to reconstruct $\overline{C}$ around the PS seems an original contribution to CFD.

Some code features validated in Amicarelli (2024, [18]) are provided with detailed descriptions in the current paper, as they are active and further tested with the new simulations. It is the SPH quadrature formulae and the spatial reconstruction schemes for the mean pressure, the mean TKE and the mean concentration at the PS. The SPH spatial filters of a generic function, gradient and 'quasi-Laplacian' consider contributions from fluid particles, solid particles and fixed-wall elements. The SPH quadrature formulae rely on the assessment of relative positions, kernel functions and gradients, and are also computed over the barycentres of the positioning grid and the monitoring points. It is demonstrated that each SPH filter represents a spatial filter in the continuum plus a 3D open weighted quadrature formula for given irregular nodes. The formulations for all the SPH-TSE ensemble statistics and the SPH spatial statistics of the code are presented. The approximations of gradients and functions are systematically assessed by C_1-consistent SPH quadrature formulae in the BE terms and the spatial reconstruction schemes, including boundary contributions in the renormalisation matrix, whereas SPH models usually adopt C_0-consistent approximations with few and partial exceptions (e.g., Marongiu et al. 2010, [62]; Lind et al., 2012, [63]; Amicarelli et al. 2017, [64]; Khayyer et al., 2018, [65]; Chen et al., 2022, [34]). Unlike the mesh-based CFD codes for Air Quality (e.g. Efthimiou et al., 2016, [48]), the code of Sec.2 adopts a more approximated emission scheme to represent the Pollutant Source, exploiting the SPH Lagrangian approach.

The pre-processing procedures for the inlet mean-TKE dissipation rate and the depth of the turbulent Boundary Layer are also reported. The code simulations show limited elapsed times even if the executions only used 3.5 physical cores due to a very-low-cost operative strategy. Concentration turbulent fluctuations are neglected; they are relevant in case of non-linear relationships between concentration and damage as for odour dispersion (e.g. Viccione et al., 2014, [66]).

Acknowledgements

This study received no public funding. Formal details on the code CFD-OUT-sweePDF v.2.0.0 (Amicarelli et al.) are reported at https://www.researchgate.net/profile/Andrea-Amicarelli and github.com/AndreaAmicarelli-personal. Videos on the results of CFD-OUT-sweePDF are published at https://www.youtube.com/@andrea.amicarelli. Regarding those source-code parts which were imported in CFD-OUT-sweePDF v.1.0.0 (Amicarelli et al.) from SPHERA v.10.0.0 (RSE SpA) — as mentioned in the last lines of Sec.2, Sec.3.4 and Sec.3.6, with detailed references to the associated papers — the following notice applies: 'SPHERA v.10.0.0 was realised by RSE SpA thanks to the funding "Fondo di Ricerca per il Sistema Elettrico" within the frame of a Program Agreement between RSE SpA and the Italian Ministry of Economic Development (Ministero dello Sviluppo Economico)'.

Disclosure statement

The author reports there are no competing interests to declare.

10. APPENDIX: PRE-PROCESSING PROCEDURES

Two general pre-processing procedures for the code of Sec.2 are executed in the current study as well as in Amicarelli (2024, [18]) and Amicarelli (2025, [19]). They concern the inlet mean-TKE dissipation rate (Sec.10.1) and the depth of the turbulent boundary layer (Sec.10.2).

10.1. Inlet mean-TKE dissipation rate

The inlet values for the mean-TKE dissipation rate $\overline{\varepsilon}$ can be set following five alternative formulae:

$$\overline{\varepsilon}=\begin{cases}\dfrac{u_*^3}{k_v r},\ \dfrac{11\overline{\nu}}{u_*}<r\le\delta_{NSBL,\overline{\varepsilon}}\\ 0,\ 0<r\le\dfrac{11\overline{\nu}}{u_*}\end{cases};\ \overline{\varepsilon}=\max\left\{0.6\overline{q}\left[\left(-\overline{S}_m\right)R_m\right]^{\frac{1}{4}};\overline{\varepsilon}_{\lim}\right\},\ \overline{\varepsilon}_{\lim}=\frac{1}{2}\sqrt{\frac{3}{2}}\frac{\left(C_\mu\right)^{\frac{3}{4}}\sigma_w\overline{q}}{k_v r};\tag{10.1}$$

$$\overline{\varepsilon}=\max\left\{0.6\overline{q}\sqrt{-\overline{S}_m};\overline{\varepsilon}_{\lim}\right\};\ \overline{\varepsilon}=\max\left\{-\overline{u'w'}\frac{\partial\overline{u}}{\partial z};\overline{\varepsilon}_{\lim}\right\};\ \overline{\varepsilon}=\frac{u_*^3}{k_v r}\left(1-\frac{r}{\delta_T}\right)^{\frac{3}{2}},\delta_{NSBL,\overline{\varepsilon}}<r\le\delta_T$$

where k_v is von Karman constant and σ_w (m/s) is the standard deviation of the vertical velocity; δ_{NSBL} (m) and δ_T (m) are the depths of the Neutral Surface Boundary Layer (NSBL) and the Turbulent BL. The first formulation in (10.1) is used as WF in the code of Sec.2 (Amicarelli, 2024, [18]). The two following formulations are the closed-form solutions of TKE-BE under homogeneous and stationary turbulence, according to either Kat&Lau-k-eps turbulence closure (Sec.2) or k-eps model (commonly used in CFD for atmospheric flows, e.g. Efthimiou et al., 2021, [67]). A limiter '$_{lim}$' applies to avoid unphysical underestimations of $\overline{\varepsilon}$, incoherent with the distance from the fixed wall r (m); it involves an approximate value of the Eulerian integral time scale of turbulence in the NSBL. The limiter is imposed only where necessary to minimise the corrections to the raw experimental input data. The fourth expression assumes a simplified 1D TKE-BE and the 3D definition of the friction velocity u_* (m/s), without assumptions on the mean-velocity gradient. The last formula in (10.1) can be derived for the Neutral Outer Boundary Layer (NOBL) as in Amicarelli (2024, [18]). The formulations in (10.1) are reported in order of decreasing priority, considering their accuracy and coherence with the rest of the code. Such order can be revised according to the actual availability and reliability of the experimental data. In case of 2D simulations with 1D mean flow, the fourth expression is preferred to the previous two ones. If $\overline{q}$ BCs and ICs are set in terms of WF or NOBL profile, it is suggested to coherently apply the analogous profiles of $\overline{\varepsilon}$, unless measurements indicate otherwise.

10.2. An operative definition for the depth of the turbulent Boundary Layer

The depth of the turbulent Boundary Layer δ_T, requested to assess δ_{NSBL} for the WFs of the code (Sec. 2) and for other pre-processing procedures, is provided as an input value. The following operative definition was used in Amicarelli (2024, [18]) as function of the distance from the wall r (m):

$$\delta_T=\min_i\left\{r_i\right\},\ r_1=\min_j\left\{r_j:\frac{\overline{u}_\tau\big|_{r_j}}{\overline{u}_\tau\big|_{0.3r_j}}=1.1\right\},\ r_2=\min_j\left\{r_j:u_*^2\big|_{r_j}\le0.05u_*^2\big|_{r_{\min}}\right\},$$
$$r_3=\min_j\left\{r_j:\overline{q}\big|_{r_j}\le0.05\overline{q}\big|_{r_{\min}}\right\},\ r_4=\min_j\left\{r_j:\sigma_u\big|_{r_j}\le0.05\sigma_u\big|_{r_{\min}}\right\},\tag{10.2}$$
$$r_5=\min_j\left\{r_j:\sigma_v\big|_{r_j}\le0.05\sigma_v\big|_{r_{\min}}\right\},\ r_6=\min_j\left\{r_j:\frac{\partial\overline{u}_\tau}{\partial r}\bigg|_{r_j}>0\right\},\ r_7=\min_j\left\{r_j:\mathrm{Re}_T\big|_{r_j}\le0.05\right\}$$

whose minima can be assessed over the inlet section, for sake of simplicity; $\overline{u}_\tau$ (m/s) is the tangential-to-wall component of the mean velocity, σ_i (m/s) is a standard deviation of velocity. The distance r_1

is consistent with the WFs reported in Amicarelli (2024, [18]). The distance r_6 is useful if the fluid-wall relative velocity changes direction not far from the wall, under complex flows. The following definition of the friction velocity in the BL $\left(u_{*,r}^2 \equiv -\overline{u'w'}\Big|_r\right)$ might be useful to assess the quantities in (10.2), which does not need any WF to be computed. Besides any simple operative definition of δ_T for a CFD code, thorough analyses on the evolution of the Boundary Layer depth are available in specific studies (e.g., Moroni & Cenedese, 2006, [68]; Catalano et al., 2012, [69]).

REFERENCES

[1] Y. Tominaga and T. Stathopoulos, "Turbulent Schmidt numbers for CFD analysis with various types of flowfield," *Atmospheric Environment,* vol. 41, no. 37, pp. 8091-8099, https://doi.org/10.1016/j.atmosenv.2007.06.054, 2007.

[2] G. Efthimiou, S. Andronopoulos, R. Tavares and J. Bartzis, "CFD-RANS prediction of the dispersion of a hazardous airborne material released during a real accident in an industrial environment," *Journal of Loss Prevention in the Process Industries,* vol. 46, pp. 23-36, http://dx.doi.org/10.1016/j.jlp.2017.01.015, 2017.

[3] A. Venetsanos, E. Papanikolaou and J. Bartzis, "The ADREA-HF CFD code for consequence assessment of hydrogen applications," *Int. J. Hydrog. Energy,* vol. 35, pp. 3908-3918, 2010.

[4] D. Violeau, "Explicit algebraic Reynolds stresses and scalar fluxes for density-stratified shear flows," *Phys. Fluids,* vol. 21, p. 035103, 2009.

[5] K.-J. Hsieh, F.-S. Lien and E. Yee, "Numerical modeling of passive scalar dispersion in an urban canopy layer," *Journal of Wind Engineering and Industrial Aerodynamics,* vol. 95, pp. 1611–1636, doi:10.1016/j.jweia.2007.02.028, 2007.

[6] L. Dong, H. Zuo, L. Hu, B. Yang, L. Li and L. Wu, "Simulation of heavy gas dispersion in a large indoor space using CFD model," *Journal of Loss Prevention in the Process Industries,* vol. 46, pp. 1-12, https://doi.org/10.1016/j.jlp.2017.01.012, 2017.

[7] A. Issakhov, A. Alimbek and A. Issakhov, "A numerical study for the assessment of air pollutant dispersion with chemical reactions from a thermal power plant," *Engineering Applications of Computational Fluid Mechanics,* vol. 14, no. 1, pp. 1035-1061, https://doi.org/10.1080/19942060.2020.1800515, 2020.

[8] J. Fackrell and A. Robins, "Concentration fluctuations and fluxes in plumes from point sources in a turbulent boundary layer," *Journal of Fluid Mechanics,* vol. 117, p. 1–26, 1982.

[9] J.-J. Baik, Y.-S. Kang and J.-J. Kim, "Modeling reactive pollutant dispersion in an urban street canyon," *Atmospheric Environment,* vol. 41, pp. 934–949, doi:10.1016/j.atmosenv.2006.09.018, 2007.

[10] Y. Tominaga, S. Iizuka, M. Imano, H. Kataoka, A. Mochida, T. Nozu, Y. Ono, T. Shirasawa, N. Tsuchiya and R. Yoshie, "Cross Comparisons of CFD Results of Wind and Dispersion Fields for MUST Experiment: Evaluation Exercises by AIJ," *Journal of Asian Architecture and Building Engineering,* vol. 12, no. 1, pp. 117–124, https://doi.org/10.3130/jaabe.12.117, 2013.

[11] E. Yee and C. Biltoft, "Concentration fluctuation measurement in a plume dispersing through a regular array of obstacles," *Boundary-Layer Meteorology,* vol. 111, pp. 363-415, https://doi.org/10.1023/B:BOUN.0000016496.83909.ee, 2004.

[12] S. B. Pope, "PDF methods for turbulent reacting flows," *Progress in Energy and Combustion Science,* vol. 11, p. 119–192, 1985.

[13] P. M. Morkisz and P. Przybylowicz, "Optimal pointwise approximation of SDE's from inexact information," *Journal of Computational and Applied Mathematics,* vol. 324, pp. 85–100, http://dx.doi.org/10.1016/j.cam.2017.04.023, 2017.

[14] M. Bahlali, E. Dupont and B. Carissimo, "A hybrid CFD RANS/Lagrangian approach to model atmospheric dispersion of pollutants in complex urban geometries," *Int. J. Environ. Pollut.,* vol. 64, no. 1-3, pp. 74-89, DOI https://doi.org/10.1504/IJEP.2018.099150, 2018.

[15] M. Bahlali, E. Dupont and B. Carissimo, "Atmospheric dispersion using a Lagrangian stochastic approach: application to an idealized urban area under neutral and stable meteorological conditions," *J Wind Eng Ind Aerodyn,* vol. 193, no. 103976, p. DOI https://doi.org/10.1016/j.jweia.2019.103976, 2019.

[16] C. Gariazzo, A. Pelliccioni, M. Bogliolo and et al., "Evaluation of a Lagrangian Particle Model (SPRAY) to Assess Environmental Impact of an Industrial Facility in Complex Terrain," *Water, Air, & Soil Pollution,* vol. 155, pp. 137–158, https://doi.org/10.1023/B:WATE.0000026525.82039.ef, 2004.

[17] G. Taylor, "Diffusion by continuous movements," *Proceedings of the London Mathematical Society,* Vols. s2-20, no. 1, pp. 196-212, https://doi.org/10.1112/plms/s2-20.1.196, 1922.

[18] A. Amicarelli, "A Lagrangian RANS CFD-SPH code for turbulent flows with pollutant transport and applications to Outdoor/Indoor/Duct Air Quality," *International Journal of Computational Fluid Dynamics,* vol. 38, no. 5, p. 339–376; https://doi.org/10.1080/10618562.2025.2469497, 2024.

[19] A. Amicarelli, "RANS SPH CFD for micro-scale meteorology and Air Quality in and around Urban Canopies," *paper preprint,* pp. 1-30, protocol, RS2502, 2025.

[20] A. Amicarelli, G. Leuzzi, P. Monti and D. J. Thomson, "A comparison between IECM and IEM Lagrangian models," *International Journal of Environment and Pollution,* vol. 44, no. 1/2/3/4, pp. 324-331, DOI 10.1504/IJEP.2011.038433, 2011.

[21] D. Isik and Z. He, "SPH Viscous Flow Around a Circular Cylinder: Impact of Viscous Formulation and Background Pressure," *International Journal of Computational Fluid Dynamics,* vol. 35, no. 6, pp. 451-467, DOI: 10.1080/10618562.2021.1979523, 2021.

[22] J. Galindo, R. Navarro, L. M. García-Cuevas, D. Tarí, H. Tartoussi and S. Guilain, "A zonal approach for estimating pressure ratio at compressor extreme off-design conditions," *International Journal of Engine Research,* vol. 20, no. 4, pp. 393-404, https://doi.org/10.1177/1468087418754899, 2018.

[23] R. Vignjevic and J. Campbell, "Review of Development of the Smooth Particle Hydrodynamics (SPH) Method," in *Predictive Modeling of Dynamic Processes*, Boston, Springer, S. Hiermaier (ed.), 2009, pp. 367-396, https://doi.org/10.1007/978-1-4419-0727-1_20.

[24] A. Crespo, M. Gómez-Gesteira and R. Dalrymple, "Modeling Dam Break Behavior over a Wet Bed by a SPH Technique," *Journal of Waterway, Port, Coastal and Ocean Engineering,* vol. 134, no. 6, pp. 313-320, https://doi.org/10.1061/(ASCE)0733-950X(2008)134:6(313), 2008.

[25] F. Aristodemo, S. Marrone and I. Federico, "SPH modeling of plane jets into water bodies through an inflow/outflow algorithm," *Ocean Engineering,* vol. 105, pp. 160-175, https://doi.org/10.1016/j.oceaneng.2015.06.018, 2015.

[26] X. Cui, W. G. Habashi and V. Casseau, "Multiphase SPH Modelling of Supercooled Large Droplets Freezing on Aircraft Surfaces," *International Journal of Computational Fluid Dynamics,* vol. 35, no. (1-2), pp. 79-92, https://doi.org/10.1080/10618562.2020.1817401, 2020.

[27] L. Fang, S. Wang and J. Hong, "Analytical expressions of the deformation limit of fluid particles," *Physics Letters A,* vol. 381, pp. 3996–4004, https://doi.org/10.1016/j.physleta.2017.10.032, 2017.

[28] X. Cui, A. Bakkar and W. G. Habashi, "A multiphase SPH framework for supercooled large droplets dynamics," *International Journal of Numerical Methods for Heat & Fluid Flow,* vol. 29, no. 7, pp. 2434-2449, https://doi.org/10.1108/HFF-10-2018-0547, 2019.

[29] B. Tagliafierro, M. Karimirad, I. Martínez-Estévez, J. M. Domínguez, G. Viccione and A. J. C. Crespo, "Numerical Assessment of a Tension-Leg Platform Wind Turbine in Intermediate Water Using the Smoothed Particle Hydrodynamics Method," *Energies,* vol. 15, no. 3993, pp. 1-23, https://doi.org/10.3390/en15113993, 2022.

[30] A. Issakhov and A. Baitureyeva, "Modeling of a passive scalar transport from thermal power plants to atmospheric boundary layer," *International Journal of Environmental Science and Technology,* vol. 16, no. 8, pp. 4375-4392, https://doi.org/10.1007/s13762-019-02273-y, 2019.

[31] A. Leroy, D. Violeau, M. Ferrand and C. Kassiotis, "Unified semi-analytical wall boundary conditions applied to 2-D incompressible SPH," *Journal of Computational Physics,* vol. 261, pp. 106–129, http://dx.doi.org/10.1016/j.jcp.2013.12.035, 2014.

[32] B. Launder and D. Spalding, “The numerical computation of turbulent flows,” *Comput. Meth. Applied Mech. Eng.,* vol. 3, no. 2, pp. 269-289, 1974.

[33] L. Fang, H.-K. Zhao, L.-P. Lu, Y.-W. Liu and H. Yan, “Quantitative description of non-equilibrium turbulent phenomena in compressors,” *Aerospace Science and Technology,* vol. 71, pp. 78-89, https://doi.org/10.1016/j.ast.2017.09.20, 2017.

[34] Y.-k. Chen, D. D. Meringolo and Y. Liu, “SPH study of wave force on simplified superstructure of open-type sea access road,” *Ocean Engineering,* vol. 249, no. 110869, pp. 1-30, https://doi.org/10.1016/j.oceaneng.2022.110869, 2022.

[35] A. Di Monaco, S. Manenti, M. Gallati and S. Sibilla, “SPH modeling of solid boundaries through a semi-analytic approach,” *Engineering Applications of Computational Fluid Mechanics,* vol. 5, no. 1, pp. 1-15, DOI: 10.1080/19942060.2011.11015348, 2011.

[36] SPHERA (RSE SpA), “https://github.com/GiordanoAgateRSE/SPHERA,” 2022. [Online].

[37] A. Amicarelli, R. Albano, D. Mirauda, G. Agate, A. Sole and R. Guandalini, “A Smoothed Particle Hydrodynamics model for 3D solid body transport in free surface flows,” *Computers & Fluids,* vol. 116, p. 205–228; DOI 10.1016/j.compfluid.2015.04.018, 2015.

[38] A. Amicarelli, S. Manenti, R. Albano, G. Agate, M. Paggi, L. Longoni, D. Mirauda, L. Ziane, G. Viccione, S. Todeschini, A. Sole, L. Baldini, D. Brambilla, M. Papini, M. Khellaf, B. Tagliafierro, L. Sarno and G. Pirovano, “SPHERA v.9.0.0: a Computational Fluid Dynamics research code, based on the Smoothed Particle Hydrodynamics mesh-less method,” *Computer Physics Communications,* vol. 250, pp. 107157, https://doi.org/10.1016/j.cpc.2020.107157, 2020.

[39] A. Amicarelli, S. Manenti and M. Paggi, “SPH modelling of dam-break floods, with damage assessment to electrical substations,” *International Journal of Computational Fluid Dynamics,* vol. 35, no. 1-2, pp. 3-21; DOI 10.1080/10618562.2020.1811240, 2021.

[40] A. Amicarelli, E. Abbate and A. Frigerio, “SPH modelling of a dike failure with detection of the landslide sliding surface and damage scenarios for an electricity pylon,” *International Journal of Computational Fluid Dynamics,* vol. 36, no. 4, pp. 265-293, DOI 10.1080/10618562.2022.2108020, 2022.

[41] B. Tagliafierro, S. Mancini, P. Ropero-Giralda, J. M. Domínguez, A. J. C. Crespo and G. Viccione, “Performance Assessment of a Planing Hull Using the Smoothed Particle Hydrodynamics Method,” *J. Mar. Sci. Eng.,* vol. 9, no. 244, pp. 1-18, https://doi.org/10.3390/jmse9030244, 2021.

[42] R. W. Randles and L. D. Libertsky, “Smoothed Particle Hydrodynamics. Some recent improvements and applications,” *Comput. Methods Appl. Mech. Engrg.,* vol. 139, pp. 375-408, 1996.

[43] M. Basa, N. Quinlan and M. Lastiwka, “Robustness and accuracy of SPH formulations for viscous flow,” *International Journal for Numerical Methods in Fluids,* vol. 60, no. 10, pp. 1127-1148, DOI: 10.1002/fld.1927, 2009.

[44] J. Monaghan and J. Lattanzio, “A refined method for astrophysical problems,” *Astronomy and Astrophysics,* vol. 149, pp. 135-143, 1985.

[45] M. Gallati and G. Braschi, “Simulazione lagrangiana di flussi con superficie libera in problemi di idraulica,” in *L’ACQUA 5*, 2000.

[46] S. Gu, X. Zheng, L. Ren, H. Xie, Y. Huang, J. Wei and S. Shao, “SWE-SPHysics simulation of dam break flows at South-Gate Gorges Reservoir,” *Water,* vol. 9, no. 6, pp. art. no. 387, https://doi.org/10.3390/w9060387, 2017.

[47] J. Cercos-Pita, M. Antuono, A. Colagrossi and A. Souto-Iglesias, “SPH energy conservation for fluid–solid interactions,” *Comput. Methods Appl. Mech. Engrg.,* vol. 317, pp. 771–791, http://dx.doi.org/10.1016/j.cma.2016.12.037, 2017.

[48] G. Efthimiou, S. Andronopoulos, I. Tolias and A. Venetsanos, “Prediction of the upper tail of concentration distributions of a continuous point source release in urban environments,” *Environmental Fluid Mechanics,* vol. 16, no. 5, pp. 899-921, DOI https://doi.org/10.1007/s10652-016-9455-2, 2016.

[49] L. Fang, L. Li, J. Guo, Y. Liu and X. Huang, “Time scale of directional change of active Brownian particles,” *Physics Letters A,* vol. 427, no. 127934, p. https://doi.org/10.1016/j.physleta.2022.127934, 2022.

[50] S. Pope, "Simple models of turbulent flows," *PHYSICS OF FLUIDS,* vol. 23, pp. 011301, 1-19, DOI: 10.1063/1.3531744, 2011.

[51] S. Pope, "The vanishing effect of molecular diffusivity on turbulent dispersion: implications for turbulent mixing and the scalar flux," *Journal of Fluid Mechanics,* vol. 359, pp. 299-312, 1998.

[52] S. Socolofsky and G. Jirka, Environmental Fluid Mechanics, Part I: Mass Transfer and Diffusion, Institut für Hydromechanik, Universität Karlsruhe, Germany, Engineering – Lectures, 2nd Edition, 2002.

[53] B. Sawford, P. Yeung and J. Hackl, "Reynolds Number Dependence of Relative Dispersion Statistics in Isotropic Turbulence," *Physics of Fluids,* vol. 20, p. 065111, 2008.

[54] S. Hanna and R. Britter, Wind Flow and Vapor Cloud Dispersion at Industrial and Urban Sites, New York: American Institute of Chemical Engineers, pp.1-208, ISBN 978-0-816-90863-9, 2002.

[55] K. Bezpalcova, Physical modelling of flow and diffusion in urban canopy; PhD thesis, Prague: Charles University, 2007.

[56] B. Cushman-Roisin, "Environmental Fluid Mechanics," 2019. [Online]. Available: http://www.dartmouth.edu/~cushman/books/EFM.html. [Accessed 21 May 2019].

[57] R. Martinuzzi and C. Tropea, "The flow around surface-mounted, prismatic obstacles placed in a fully developed channel flow," *J. Fluids Eng.,* vol. 115, pp. 85-92, https://doi.org/10.1115/1.2910118, 1993.

[58] I. Mavroidis, R. Griffiths and D. Hall, "Field and wind tunnel investigations of plume dispersion around single surface obstacles," *Atmospheric Environment,* vol. 37, pp. 2903-2918, DOI: 10.1016/S1352-2310(03)00300-5, 2003.

[59] X. Cui, W. G. Habashi and V. Casseau, "MPI Parallelisation of 3D Multiphase Smoothed Particle Hydrodynamics," *International Journal of Computational Fluid Dynamics,* vol. 34, no. 7-8, pp. 610-621, DOI: 10.1080/10618562.2020.1785436, 2020.

[60] D. Haworth, "Progress in probability density function methods for turbulent reacting flows," *Progress in Energy and Combustion Science,* vol. 36, pp. 168–259, DOI: 10.1016/j.pecs.2009.09.003, 2010.

[61] D. D. Meringolo, F. Aristodemo, S. Servidio and P. G. F. Filianoti, "Large eddy simulations of turbulence diffusion within the smoothed particle hydrodynamics," *Physics of Fluids,* vol. 36, no. 4, 045105, pp. 1-21, https://doi.org/10.1063/5.0202974, 2024.

[62] J.-C. Marongiu, F. Leboeuf, J. Caro and E. Parkinson, "Free surface flows simulations in Pelton turbines using an hybrid SPH-ALE method," *J. Hydraul. Res.,* vol. 47, pp. 40–49, DOI: 10.1080/00221686.2010.9641244, 2010.

[63] S. Lind, R. Xu, P. Stansby and B. Rogers, "Incompressible smoothed particle hydrodynamics for free-surface flows: A generalised diffusion-based algorithm for stability and validations for impulsive flows and propagating waves," *Journal of Computational Physics,* vol. 231, no. 4, pp. 1499-1523, DOI: 10.1016/j.jcp.2011.10.027, 2012.

[64] A. Amicarelli, B. Kocak, S. Sibilla and J. Grabe, "A 3D Smoothed Particle Hydrodynamics model for erosional dam-break floods," *International Journal of Computational Fluid Dynamics,* vol. 31, no. 10, pp. 413-434, DOI: 10.1080/10618562.2017.1422731, 2017.

[65] A. Khayyer, H. Gotoh, Y. Shimizu, K. Gotoh, H. Falahaty and S. Shao, "Development of a projection-based SPH method for numerical wave flume with porous media of variable porosity," *Coastal Engineering,* vol. 140, pp. 1-22; DOI: 10.1016/j.coastaleng.2018.05.003, 2018.

[66] G. Viccione, D. Spiniello, T. Zarra and V. Naddeo, "Fluid dynamic simulation of odour measurement chamber," *Chemical Engineering Transactions,* vol. 40, pp. 109-114, https://doi.org/10.3303/CET1440019, 2014.

[67] G. Efthimiou, F. Barmpas, G. Tsegas and N. Moussiopoulos, "Development of an Algorithm for Prediction of the Wind Speed in Renewable Energy Environments," *Fluids,* vol. 6, no. 461, pp. 1-9, https://doi.org/10.3390/fluids6120461, 2021.

[68] M. Moroni and A. Cenedese, "Penetrative convection in stratified fluids: velocity and temperature measurements," *Nonlin. Processes Geophys.,* vol. 13, pp. 353–363, https://doi.org/10.5194/npg-13-353-2006, 2006.

[69] F. Catalano, M. Moroni, A. Cenedese and V. Dore, “An alternative scaling for unsteady penetrative free convection,” *J. Geophys. Res.,* vol. 117, pp. D18102, https://doi.org/10.1029/2012JD018229, 2012.